Chemical Science

ROYAL SOCIETY OF CHEMISTRY

PERSPECTIVE

View Article Online
View Journal | View Issue

Cite this: *Chem. Sci.*, 2025, **16**, 15796

All publication charges for this article have been paid for by the Royal Society of Chemistry

Received 25th March 2025
Accepted 11th August 2025

DOI: 10.1039/d5sc02236c

rsc.li/chemical-science

Emission-tunable manganese(II) halides: structure–property relationships and functional applications

Chuying Wang, Yacong Li and Zhengtao Deng *

Luminescent Mn(II) complexes have attracted extensive attention owing to their properties of color tunability, high PLQYs, large Stokes shifts and thermal stability. Luminescent Mn(II) complexes can exhibit orange, green, and red emissions depending on the environment of Mn^{2+}. These various properties made Mn(II) complexes attractive candidates for different fields of applications such as LEDs and radiation detection. In this perspective, we connect the emissions of Mn(II) complexes with the corresponding crystal structure and the environment of Mn^{2+}. Then, we summarize the recent progress of luminescent Mn(II) complexes in LEDs and radiation detection. Finally, we present the challenges and outlook for future research on luminescent Mn(II) complexes.

1 Introduction

In the past few years, lead halide perovskites have become promising materials for optoelectronic devices due to their excellent optoelectronic properties.[1,2] However, their toxicity and poor stability have hindered further application in many fields.[3] One of the most effective solutions is to find nontoxic and reliable alternatives beyond lead halide perovskite.[4–6] Mn(II) halides have emerged as sustainable alternatives to lead perovskites, achieving near-unity photoluminescence quantum yield (PLQY) and enabling emission tunability to green and red luminescence through structural control. These earth-abundant systems combine luminescence efficiency with environmental compatibility, addressing demands for eco-friendly photoelectric applications.

The intrinsic luminescence of manganese halides originates from d–d electronic transitions of the manganese center, where the crystal field splitting determines emission characteristics through ligand field modulation. Manganese first emerged as a strategic luminescent dopant for host materials with a low PLQY, where its distinct electronic configuration enables efficient energy transfer pathways for photoluminescence enhancement. The Mn-doped ZnS nanocrystals (NCs) synthesized by Bhargava in 1994 are the earliest semiconductor NCs, exhibiting quantum yields of less than 20%.[7] Mn^{2+} dopants in II–VI semiconductors (*e.g.*, ZnS and CdSe) achieve tetrahedral coordination through isovalent substitution, activating spin-forbidden d–d photoluminescence *via* crystal field engineering.[8] Since then, a great diversity of Mn-doped II–VI semiconductor NCs have been explored and applied to biomedical imaging,[9] white light emitting diodes,[10] solar cells,[11] radiation detection[12] and luminescent solar concentrators.[13] Given the great potential for various light emission applications of Mn-doped semiconductor NCs, metal halide perovskite NCs have also been developed as the latest semiconductor hosts of Mn(II) dopant. In 2016, Mn-doped $CsPbX_3$ perovskite NCs were almost simultaneously synthesized by Parobek *et al.*[14] and Liu *et al.*[15] *via* a modified hot injection process.

Besides being a dopant, Mn can also serve as an independent luminescent center without doping. Luminescent Mn(II) halide complexes, as some of the emerging lead free materials, have been intensively investigated over the past decades owing to their properties of tunable emission, high PLQYs, large Stokes shifts, good thermal stability and low toxic nature compared to lead halide perovskites. In recent years, various luminescent Mn(II) halide complexes have been designed and synthesized. According to the coordination environment of the Mn^{2+} center Mn(II) halides can be classified into four-fold-coordinated, $[MnX_4]^{2-}$, and six-fold-coordinated, $[MnX_6]^{4-}$, manganese halide complexes. Based on the emission wavelength, Mn(II) halides can be classified into green and red Mn(II) phosphors. By their crystal structure, Mn(II) complexes are further classified into zero-, one- and two-dimensional structures. The diversity of Mn(II) halide complexes leads to their different photoelectric properties, which can be applied in different fields. For example, Ju *et al.* fabricated a white LED (WLED) exhibiting a luminous efficacy of up to 96 lm W^{-1} using green $(C_5H_6N)_2MnBr_4$ and red $C_5H_6NMnCl_3$ phosphors on a blue chip, reflecting the high PLQY and good thermal stability of these manganese(II) complexes.[16] Wang *et al.* prepared a pure red LED with $(ABI)_4MnBr_6$ showing the maximum recording brightness of 4700 cd m^{-2} and an EQE of 9.8%, suggesting the excellent electroluminescence (EL) performance of this complex.[17] Besides their use in LEDs, Mn(II) complexes can also be applied

College of Engineering and Applied Sciences, State Key Laboratory of Analytical Chemistry for Life Science, National Laboratory of Micro-structures, Nanjing University, Nanjing, Jiangsu, 210023, P. R. China. E-mail: dengz@nju.edu.cn

in radiation detection. A Mn-doped $(C_{18}H_{37}NH_3)_2PbBr_4$ scintillator was finally made into imaging plates for fast neutron radiography with 0.5 lp mm^{-1} spatial resolution.[18] Ma *et al.* synthesized an X-ray scintillator $(C_{38}H_{34}P_2)MnBr_4$ with a high light yield of 80 000 photon per MeV, and a low detection limit of 72.8 nGy s^{-1}, indicating the potential of manganese(II) complexes in X-ray imaging.[19]

According to previous research, the emission of Mn from both the dopant and Mn(II) halide complexes was due to the $^4T_1(G) \rightarrow {}^6A_1(S)$ transition of Mn^{2+}. The environment of Mn^{2+} in different structures leads to differences in the luminescent properties. In this perspective, we have summarized recent progress in luminescent Mn(II) complexes. We relate the luminescent properties of Mn(II) complexes to their corresponding environment and crystal structures. Then, we discuss their applications in LEDs and X-ray imaging. Finally, we present an outlook for the future development for Mn(II) halides.

2 Structures and properties of Mn halides

2.1 Emission of Mn-doped perovskite NCs

The electronic structure of Mn^{2+} in crystalline environments was analyzed through Tanabe–Sugano theory, incorporating electron correlations and crystal field (CF) effects.[20] Cubic CF splitting partially lifts degeneracies of the ^4G, ^4P, and ^4D terms, generating distinct $^4T_1(G)$, $^4T_2(G)$, $^4A_1(G)$, $^4E(G)$, $^4T_2(D)$, $^4E(D)$, and $^4T_1(P)$ states, which will be discussed in Sections 2.3 and 2.2 in detail. Mn^{2+} photoluminescence originates from the $^4T_1(G) \rightarrow {}^6A_1(S)$ transition within visible wavelengths.[21–23] The emission energy depends on the CF strength, enabling chromatic tuning across host matrices *via* ligand field engineering.

For Mn as the dopant, manganese(II) ions are incorporated into metal halide hosts through substitutional doping strategies, where their luminescent activation emerges from coordination-tuned crystal field splitting. The emission characteristics are governed by the ligand-field symmetry coordination environment of the host. For instance, Mn^{2+} substitution in tetrahedral $[ZnX_4]^{2-}$ units yields green emission under T_d-symmetry crystal field splitting,[24,25] while octahedral coordination in $[CdCl_6]^{4-}$ environments generates distinct red luminescence through O_h-symmetry crystal field effects.[26]

Recently, Mn^{2+} doped $CsPbCl_3$ perovskites exhibit tunable dual-band emission through structural confinement-mediated energy transfer, enabling applications in white-light-emitting diodes (WLEDs),[27] luminescent solar concentrators (LSCs),[28] and anti-counterfeiting[29] technologies. Fig. 1a shows that Mn-doped $CsPbCl_3$ NCs have a distinct dual emission behavior consisting of a narrow PL band at ~400 nm (blue–violet) and a broad PL band at ~600 nm (yellow–orange emission). The former is generally attributed to host band edge exciton recombination and the latter to ligand field transition ($^4T_1(G) \rightarrow {}^6A_1(S)$) of Mn^{2+} ions. Since the transition is spin-forbidden, the Mn dopant luminescence in perovskite NCs is accompanied by a microsecond or millisecond lifetime, consistent with Mn-doped II–VI semiconductor NCs.[30]

2.1.1 Bandgap-dependent PL of Mn-doped perovskite NCs. The emission of Mn-doped $CsPbX_3$ perovskite NCs is host bandgap-dependent. Fig. 1b depicts the energy level alignment of $CsPbX_3$ perovskite and Mn^{2+} ion d-state. In the case of Mn-doped $CsPbCl_3$ NCs, the photo-generated exciton has the highest band gap energy and favours the forward energy transfer from band edge to the Mn^{2+} excited state, which ultimately contributes to the introduction of Mn^{2+} ion radiative pathway.[15] However, the band gap energy of Br-based or I-based

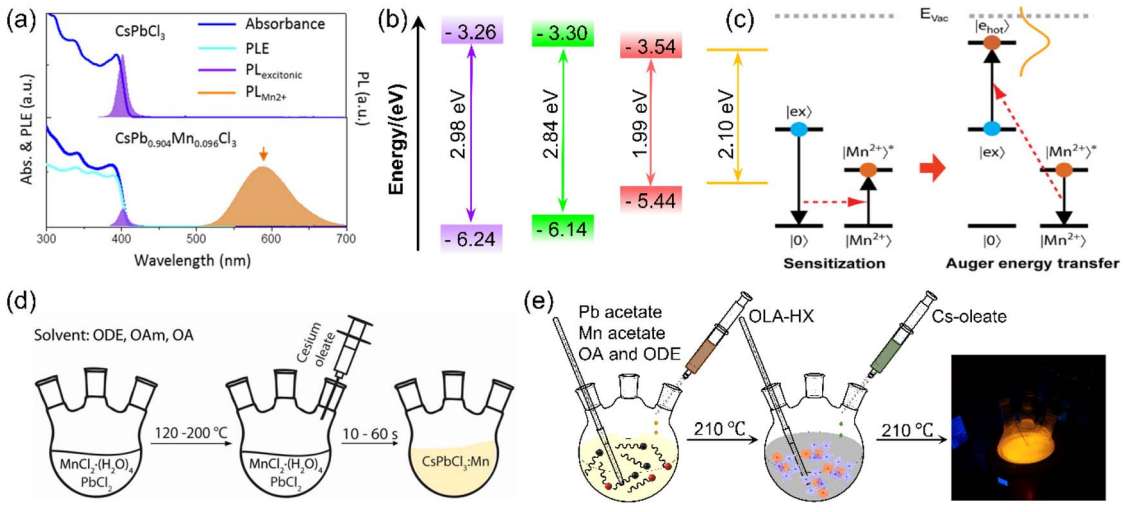

Fig. 1 (a) The optical properties of undoped (top) and Mn-doped (bottom) $CsPbCl_3$ NCs. (b) Band gap structure of $CsPbX_3$ and Mn d-states. (c) Photophysical pathways of hot electron up-conversion. $|0\rangle$ and $|ex\rangle$ are ground and exciton states of the host NCs, respectively. $|Mn^{2+}\rangle$ and $|Mn^{2+}\rangle^*$ are ground and excited states of dopants, respectively. $|e_{hot}\rangle$ represents the state generating hot electrons. E_{vac} is the vacuum level. Schematic diagram of the synthesis of Mn-doped $CsPbX_3$ NCs *via* (d) one-step hot injection and (e) two-step hot-injection processes. (a) Reproduced with permission from ref. 15. Copyright 2016, American Chemistry Society. (c) Reproduced with permission from ref. 34. Copyright 2021, American Chemistry Society. (d) Reproduced with permission from ref. 14. Copyright 2016, American Chemistry Society.

perovskite NCs is close to that of the Mn^{2+} excited state and hinders the energy transfer process, resulting in inefficient dopant emission, as observed in Mn-doped $CsPbBr_3$ and $CsPbI_3$ NCs.[31,32] Fortunately, the quantum confinement effect provides a new chance for obtaining Mn emission in non-Cl-based perovskite NCs. For example, Parobek *et al.* directly synthesized dual-emitting $CsPbBr_3$ nanocubes (6.5 nm) and nanoplatelets (NPLs, thickness: 2 nm) with confined size (7 nm) *via* the preformation of $A_2[Pb_{1-x}Mn_x]Br_4$ (A = alkylammonium).[31] The interesting thing is that dopant emission dominates in Mn-doped $CsPbBr_3$ NPLs, in contrast to stronger host emission in Mn-doped $CsPbBr_3$ nanocubes, indicating more stable exciton–dopant exchange interaction due to the enhanced confinement effect in NPLs. Furthermore, Wang *et al.* first reported the hot electron up-conversion process in quantum confined Br-based perovskite NCs and NPLs.[33] As shown in Fig. 1c, hot electrons are generated by the Auger energy transfer from excited Mn^{2+} ions to another exciton. When the energy exceeds the threshold, hot electrons can undergo long-range transfer and improve the catalytic efficiency.[34]

2.1.2 Concentration-dependent PL of Mn-doped perovskite NCs. Mn^{2+} ion doping concentration is also capable of tailoring the emission of Mn-doped $CsPbX_3$ perovskite NCs. Liu *et al.* synthesized $CsPb_xMn_{1-x}Cl_3$ perovskite NCs through adding excess $MnCl_2$ dopant into the solution and elevating the temperature, where Mn dopant emission was tuned from 569 nm to 587 nm with the increase of doping concentration from 3% to 46%.[35] The red shift of Mn dopant emission was attributed to enhanced Mn^{2+}–Mn^{2+} interaction, which come under observation in most Mn-doped systems.[36–40] In addition, as the doping concentration increases, the PLQYs of Mn-doped $CsPbCl_3$ perovskite NCs first increases then decreases. A plausible explanation is that there is an optimal Mn doping concentration in $CsPbCl_3$ perovskite NCs, which not only can ensure enough Mn^{2+} ions to compete with the exciton recombination and yield intense Mn emission but also fail to cause serious PL quenching by forming Mn^{2+}–Mn^{2+} pairs and causing nonradiative defects and deformation of the crystal structure at high Mn doping concentrations.[41] Therefore, numerous efforts have been focused on controlling the doping concentration and improving the PLQYs of Mn-doped $CsPbCl_3$ perovskite NCs.[35,40–45]

2.1.3 Improved doping and emission efficiency. At present, the majority of Mn-doped $CsPbX_3$ perovskite NCs are synthesized *via* a modified hot injection approach proposed by Protesescu *et al.*[46] Fig. 1d presents a typical synthesis process; Mn-doped perovskite NCs are formed after injecting Cs oleate into a solution containing metal halide salts ($PbCl_2$ and $MnCl_2$). However, metal halide salts are of low solubility in nonpolar solvents,[47] thus resulting in low doping efficiency (Table 1). Moreover, since the ratio of cations to anions is fixed at the stoichiometric ratio of metal halide salts, it is not possible to precisely tune the composition of Mn-doped perovskite NCs. In particular, it is difficult to create an environment with rich halide ions, which has been proved to favour the formation of Mn-doped $CsPbX_3$ perovskite NCs with high stability and improved PLQY.[48–51] To promote doping and emission efficiency of Mn-doped $CsPbX_3$ perovskite NCs, the authors recently proposed a novel "two step hot injection approach".[52] As shown in Fig. 1e, metal acetate salts (Pb acetate and Mn acetate) with good solubility in a solution containing oleic acid are chosen as the Pb source and Mn source, respectively. The first step is to inject an excessive amount of alkylamine halide salts and induce the formation of $[PbX_6]^{4-}$ clusters and $[PbX_6]^{4-}$ clusters with a high coordination number. The second step is to inject Cs oleate, which can make clusters grow into Mn-doped perovskite NCs. In our method, all sources are independent of each other, so the composition of the final NCs is completely

Table 1 Synthesis information on Mn-doped perovskite nanocrystals

Materials	Precursors	Mn : Pb	Temp/°C	Method	Doping/%	QY/%	References
$CsPbCl_3$: Mn NCs	$MnCl_2$, $PbCl_2$, and TOP	2.5 : 1	185	Hot injection	9.6	27	15
	$MnCl_2$, $PbCl_2$, and TOP	0.4 : 1	185	Hot injection	12	27	40
	$MnCl_2$, $PbCl_2$, and TOP	2 : 1	150	Hot injection	3.1	58.8	130
	$MnCl_2$, $PbCl_2$, TOP, and RNH_3Cl	0.05 : 1	180	Hot injection	1.3	27	131
	$MnCl_2$, $PbCl_2$, TOP, and RNH_3Cl	1 : 1	190	Microwave	6.5	65	132
	$MnOAc_2$, $PbOAc_2$, and RNH_3Cl	0.4 : 1	210	Hot injection	17.3	84.4	133
	$MnCl_2$, $PbCl_2$, TOP, and $CuCl_2$	0.2 : 1	260	Hot injection	2	68	50
	$MnCl_2$, $PbCl_2$, TOP, and $NiCl_2$	1 : 1	190	Hot injection	1.97	70	134
	$MnCl_2$ and $PbCl_2$	1.4 : 1	200	Hot injection	0.2	60	14
	$MnCl_2$ and $PbCl_2$	10 : 1	170	Hot injection	27	54	35
	$MnCl_2$ and $PbCl_2$	0.6 : 1	150	Hot injection	5.8	12.7	42
	$MnCl_2$ and $PbCl_2$	5 : 1	RT	LARP	28	41	135
	$MnCl_2$ and $PbCl_2$	0.6 : 1	200	Solvothermal	1	64.2	136
	$MnCl_2$ and $PbCl_2$	3 : 1	RT	Ultrasonication	3	26	44
	$MnCl_2$ and $PbCl_2$	2 : 1	RT	Ultrasonication	11.8	41.1	41
	$MnOAc_2$, $PbCl_2$, and TMS-Cl	1 : 1	170	Hot injection	10.3	35	49
	$MnOAc_2$, $PbOAc_2$, and HCl	0.1 : 1	RT	LARP	1.0	40	137
$CsPbCl_3$: Mn NPLs	$MnCl_2$ and $PbCl_2$	0.05 : 1	RT	LARP	0.8	20	138
	$MnCl_2$ and $PbCl_2$	1 : 1	230	Hot injection	50.4	36	38
	$MnCl_2$ and $PbCl_2$	0.8 : 1	200	Solvothermal	8.8	20.8	139

controllable. More importantly, we used Mn : Pb in a 3 : 7 molar ratio to get 17.3% doping in cubic $CsPbCl_3$ nanocubes. In fact, metal acetate salts have been reported as unsuitable dopants, but Mn-doped $CsPbCl_3$ perovskite NCs achieved the highest 48.5% doping efficiency and 84.4% quantum efficiency at the same time *via* the two-step hot injection.

In luminescent Mn-doped NCs, surface states serve as critical determinants of emission behavior.[53] At low Mn-doping conditions, $CsPbCl_3$ NCs demonstrate enhanced PL intensity with increasing Mn concentrations, a behavior directly correlated with $MnCl_2$-mediated chloride vacancy passivation during colloidal synthesis.[14] However, excessive dopant incorporation induces deterioration of PLQY in Mn-doped $CsPbCl_3$, which is due to the dominant Mn–Mn exchange interactions that supersede exciton-to-dopant energy transfer process.[40] This fundamental competition between defect passivation and dopant–dopant coupling establishes a concentration threshold for maximizing the luminescent performance.

2.2 Tetrahedral units for green emission

The green emission of Mn(II) halide complexes originates from the tetrahedrally coordinated Mn(II) units, which is mostly $[MnX_4]^{2-}$ (X = Cl, Br, I) for Mn(II) halide complexes. Tetrahedrally coordinated Mn(II) exhibits green emission, and the emission of Mn(II) tetrahedral (T_d) crystal fields has been studied for decades.[54] In a Mn(II) T_d field with oxide as ligands, green emission is obtained with a narrow FWHM.[55,56] However, the main drawbacks of the oxide ligand T_d field for Mn(II) are slow emission decay and the high reaction temperature.

In 2019, Kovalenko *et al.* synthesized a series of T_d $[MnX_4]^{2-}$ complexes with green emission. They found that the crystal field effects and spin–orbit coupling of Mn^{2+} determine the optical properties of manganese(II) complexes such as PL peak positions, FWHM and emission decay.[57]

2.2.1 Structure of Mn(II) halide complexes consisting of tetrahedral units. The formula of $[MnX_4]^{2-}$ halide complexes is usually A_2MnX_4 or $AMnX_4$. A can be an inorganic cation like Cs^+ (ref. 58) or organic cations such as organic ammonium[59–65] and phosphorus-containing[19,66,67] groups. To charge balance the Mn halide system, it should require two +1 cations[68] or one +2 cation[19] to push the $[MnX_4]^{2-}$ tetrahedron further apart.[62] $AMnX_4$ containing a divalent A-site typically incorporates phosphonium cations (*e.g.*, $(C_{40}H_{38}P_2)MnBr_4$,[69] $(C_{38}H_{34}P_2)MnBr_4$,[19] [DMAEMP]$MnCl_4$ and $[PDMIm]_2MnCl_4$ (ref. 63)), crystallizing in triclinic or monoclinic systems. A_2MnX_4 derivatives with monovalent A-site cations primarily utilize ammonium cations (*e.g.*, $(C_{10}H_{16}N)_2MnX_4$ (ref. 23 and 70) and $(C_8H_{20}N)_2MnBr_4$ (ref. 16)) or phosphonium cations (*e.g.*, $(BzTPP)_2MnBr_4$ (ref. 71) and $(BuTPP)_2MnBr_4$ (ref. 72)), typically adopting monoclinic symmetry. Both $AMnX_4$ and A_2MnX_4 are green-emissive Mn(II) halides that exhibit zero-dimensional (0D) architectures characterized by isolated $[MnX_4]^{2-}$ tetrahedral units (Fig. 2b and c).

2.2.2 Optical properties of green Mn(II) halide complexes. Optical properties of Mn(II) halide complexes, including PL, PLE and Abs, are derived from the d orbital of Mn(II) in different crystal fields. As for green $[MnX_4]^{2-}$ complexes, the splitting of the d orbital is affected by the tetrahedral field, as shown in Fig. 2d.[57,73] Excitation of green T_d Mn(II) halide complexes

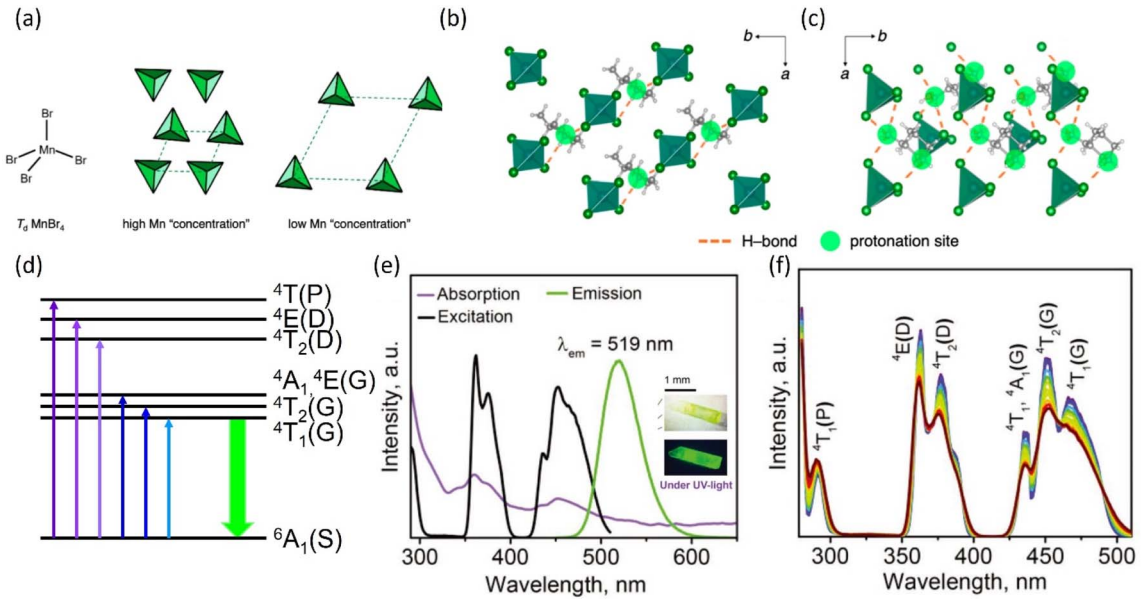

Fig. 2 Structure and luminescent properties of four-fold-coordinated $[MnX_4]^{2-}$ complexes. (a) Illustration of manganese bromide in a tetrahedral environment with short Mn–Mn distances (high Mn "concentration") and long Mn–Mn distances (low Mn "concentration"). (b) Crystal structure of A_2MnX_4 with +1 cation. (c) Crystal structure of $AMnX_4$ with +2 cation. (d) Schematic diagram showing the emission mechanism of green emissive Mn(II) halide complexes. (e) Absorption, steady-state PLE and PL spectra at 298 K and (f) temperature-dependent PLE spectra of 1R/1S Mn(II) halide complexes. (a)–(c) Reproduced with permission from ref. 62. Copyright 2020, American Chemistry Society. (e and f) Reproduced with permission from ref. 65. Copyright 2023, Wiley-VCH.

mainly comes from two transitions: group one of lower energy of $^6A_1$ to $^4T_1(G)$, $^4T_2(G)$, $^4A_1$, and $^4E(G)$ transitions and group two of higher energy of $^6A_1(S)$ to $^4T_2(D)$, $^4E(D)$, and $^4T(P)$ transitions. The group of higher energy sometimes also contains $^6A_1$ to $^4T(P)$ transition. PL emission originates from the radiative recombination from $^4T_1(G) \rightarrow {}^6A_1(S)$ transition.

For example, Seshadri *et al.* synthesized $(TMPTA)_2MnBr_4$ exhibiting green emission at 520 nm with a PLQY of 98%.[62] The excitation spectrum features two primary transitions: $^6A_1$ to $^4T_1(G)$, $^4T_2(G)$, $^4A_1$, and $^4E(G)$ (430–490 nm) and $^6A_1(S)$ to $^4T_2(D)$, $^4E(D)$, and $^4T(P)$ (350–390 nm). Artem'ev *et al.* reported R/S-$[MBA\text{-}Me_3]MnBr_4$ with emission at 519 nm (PLQY = 98%),[65] where excitation corresponds to $^6A_1$ to $^4T_1(G)$, $^4T_2(G)$, $^4A_1$, and $^4E(G)$ and $^6A_1(S)$ to $^4T_2(D)$, $^4E(D)$, and $^4T(P)$ transitions (Fig. 2e and f).[65,73] Similarly, Ma *et al.* synthesized $(C_{38}H_{34}P_2)MnBr_4$ single crystals expressing green emission (517 nm, 95%) with identical excitation characteristics.[19] The excitation spectrum has the same features as the absorption spectrum corresponding to two group transitions of blue and UV regions.

The photoluminescent properties of Mn(II) halides are governed by ligand-field splitting and spin–orbit coupling effects, which dictate emission energies and bandwidths.[57] The electron interaction between neighbouring Mn^{2+} plays an important role in the PL performance. A tendency similar to concentration quenching in Mn-doped NCs is observed in Mn(II) halides.[62] The PLQY of green $[MnX_4]^{2-}$ halide complexes is related to Mn "concentration" (Fig. 2a), which can be evaluated from the Mn–Mn distance (Fig. 3),[59,60,62,63,66,68,74,75] which is interpreted as analogous to the "concentration quenching effect" in Mn^{2+}-doped inorganic phosphors.[76] As for 0D Mn(II) complexes, the longer Mn–Mn distances weakened the nonradiative energy transfer between neighbouring Mn^{2+} centers in $[MnX_4]^{2-}$ and promoted the radiative recombination of $^4T_1(G) \rightarrow {}^6A_1(S)$ transition, achieving a higher PLQY.[63] In organic–inorganic hybrid manganese halides, photoluminescence quenching originates from nonradiative decay pathways driven by multi-phonon relaxation processes mediated through interaction between $[MnCl_4]^{2-}$ and A-cation[77] and between the Mn center and X ligands.[23]

Beyond the PLQY, the Stokes shift critically governs luminescent behavior in Mn(II) halides. Recent studies demonstrate that controlled tetrahedral distortion enables systematic emission tuning: Zhang *et al.*[78] and Qi *et al.*[79] achieved spectral shifts from green through yellow to red by modifying $[MnX_4]^{2-}$ distortions. This tunability arises from distortion-induced modulation of both crystal field splitting and electron–phonon coupling. Pronounced angular distortions reduce the $^4T_1(G)$–$^6A_1(S)$ energy gap. During triclinic-to-orthorhombic phase transitions, Br–Mn–Br angle alterations redshift emission to 555 nm with increasing Dq/B ratio.[79]

This reflects enhanced ligand field strength and decreased $^4T_1(G)$–$^6A_1(S)$ energy separation. Distorted tetrahedra intensify lattice vibrations, broadening emission linewidths from 51 nm to 68 nm *via* strengthened electron–phonon coupling.[80] Crucially, bond-angle distortions dominate these spectral modifications, while bond-length variations prove negligible.[79] The pseudohalide series further confirms this mechanism: progressive tetrahedral distortion elevates dipole moments, enhancing crystal field strength and inducing correlated emission redshifts and strengthened electron–phonon coupling, inducing bandwidth broadening.[78] Thus, angular distortion constitutes a rational design strategy for tailoring Mn(II) halide emission profiles.

In summary, the photoluminescence quantum yield (PLQY) of Mn(II) halides is primarily governed by Mn–Mn interatomic distances, which control concentration quenching effects. Concurrently, the Stokes shift is modulated by angular distortion within the crystal structure, which also dictates emission peak positions. Furthermore, bond-angle distortions and bond-length variations from organic A-site cations[23,26,81,82] influence electron–phonon coupling, determined the FWHM of luminescence.

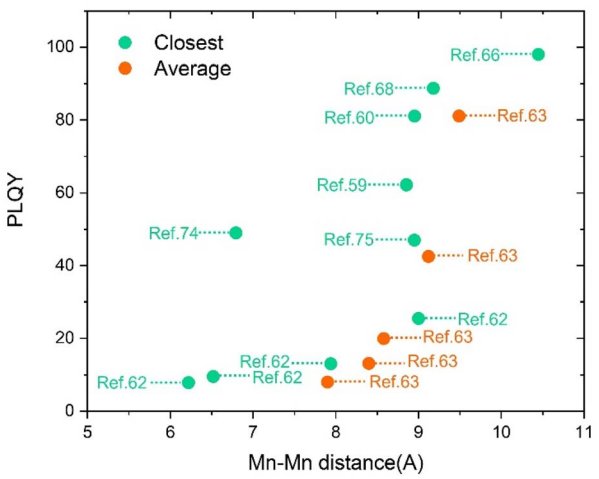

Fig. 3 Correlation between the shortest Mn–Mn distances and the PLQY. Red scatters represent samples evaluated *via* the average Mn–Mn distance and black scatters represent samples evaluated *via* the closest Mn–Mn distance.

2.3 Octahedral units for red emission

The red emission of Mn(II) complexes is derived from the six coordinated Mn(II) octahedral units, which are mostly $[MnX_6]^{4-}$ (X = Cl, Br, I) for Mn(II) halide complexes. The red emission of Mn(II) in the octahedral (O_h) crystal field mainly arises from a stronger ligand field compared to the green emission of Mn(II) in the T_d environment.[57]

2.3.1 Structure of Mn(II) halide complexes consisting of octahedral units. For red emissive Mn(II) halide complexes, the emission comes from O_h $[MnX_6]^{4-}$ units, as shown in Fig. 4a. However, different from isolated $[MnX_4]^{2-}$ units of green emissive Mn(II) halide complexes, a $[MnX_6]^{4-}$ unit can be isolated or connect to another $[MnX_6]^{4-}$ unit. According to the connection between the O_h $[MnX_6]^{4-}$ units, the structure of red emissive Mn(II) halides is crystallized to 0D, 1D and 2D structures, and the 0D structure can be further divided into an isolated structure and a partially connected structure.

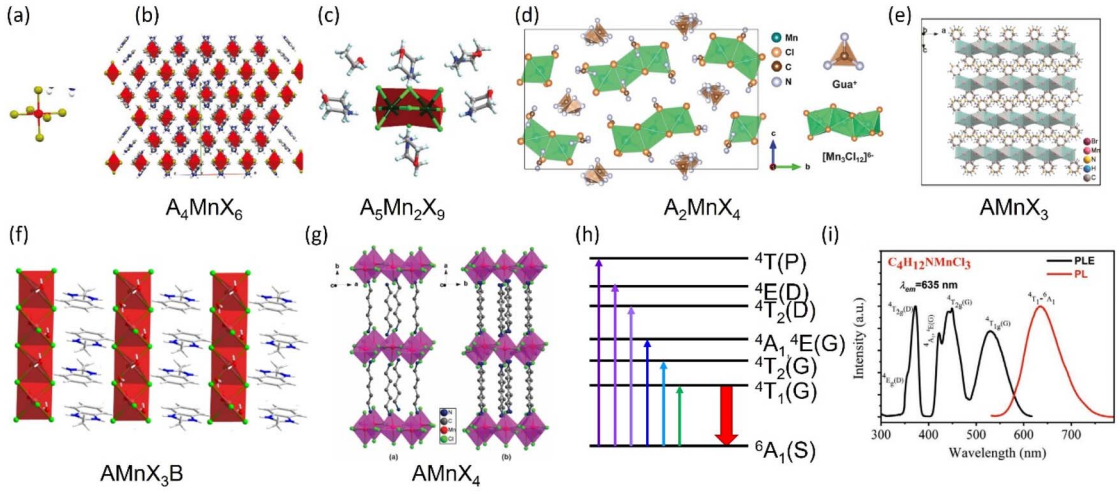

Fig. 4 Structural configurations of octahedral $[MnX_6]^{4-}$ complexes in Mn(II) halides. (a) Schematic representation of the fundamental $[MnX_6]^{4-}$ coordination unit. (b) Zero-dimensional (0D) structure featuring isolated $[MnX_6]^{4-}$ octahedra (exemplified by A_4MnX_6). (c) 0D structure containing face-sharing $[Mn_2X_9]^{5-}$ units (represented by $A_5Mn_2X_9$). (d) 0D structure with face-sharing $[Mn_3X_{12}]^{6-}$ units (A_2MnX_4). (e) One-dimensional (1D) chain structure composed of face-sharing octahedra ($AMnX_3$). (f) 1D chain structure with edge-sharing octahedra ($AMnX_3B$). (g) Two-dimensional (2D) layered structure ($AMnX_4$). (h) Schematic diagram showing the emission mechanism of red emissive Mn(II) halide complexes. (i) PLE and PL spectra of $C_4H_{12}NMnX_3$ Mn(II) halide complexes. (a and b) Reproduced with permission from ref. 17. Copyright 2021, Wiley-VCH. (c) Reproduced with permission from ref. 61. Copyright 2019, Royal Society of Chemistry. (d) Reproduced with permission from ref. 83. Copyright 2021, Wiley-VCH. (e) Reproduced with permission from ref. 84. Copyright 2018, Royal Society of Chemistry. (f) Reproduced with permission from ref. 21. Copyright 2024, American Chemical Society. (g) Reproduced with permission from ref. 92. Copyright 2016, American Chemical Society. (i) Reproduced with permission from ref. 16. Copyright 2021, Wiley-VCH.

Here, we use the formula A_mMnX_n to illustrate O_h $[MnX_6]^{4-}$ red halide complexes. A is mainly +1 or +2 cation for red $[MnX_6]^{4-}$ halide complexes. For the isolated 0D structure, the Mn^{2+} ion is surrounded by six halide ions to form a unique $[MnX_6]^{4-}$ octahedron with the formula A_4MnX_6, as shown in Fig. 4b.[17] For the partially connected 0D structure, the Mn^{2+} ion is encircled by six halide ions to form $[MnX_6]^{4-}$ octahedral units, then two or three $[MnX_6]^{4-}$ units further form a unique $[Mn_2X_9]^{5-}$ or $[Mn_3X_{12}]^{6-}$ unit by face-sharing (Fig. 4c and d).[61,83] The unit is separated by +1 cation A to form a 0D structure with the formula $A_{(n+3)}Mn_nX_{(3n+3)}$, where n stands for the number of $[MnX_6]^{4-}$ octahedra in face-sharing to form a unique $[Mn_nX_{3n+3}]^{(n+3)-}$ unit.

1D Mn(II) halide structures feature $[MnX_6]^{4-}$ octahedral units where the Mn^{2+} ions coordinate with six ligands. These octahedra form linear chains through face-sharing along specific crystallographic directions (Fig. 4e)[16,84–88] or *via* edge-sharing connection (Fig. 4f).[21,89] Face-shared 1D assemblies adopt the general formula $AMnX_3$,[85,90] while the edge-shared counterparts conform to $AMnX_3B$ (B = neutral ligands, *e.g.*, H_2O).[21,91] For the 2D structure, each Mn^{2+} is also surrounded by six X^-. The $[MnX_6]^{4-}$ octahedra share corners to form a two-dimensional network with +2 cation A occupying the space enclosed by the $[MnX_6]^{4-}$ octahedron (Fig. 4g). In the inorganic layers, each Mn atom is surrounded by six Cl atoms, in which four equatorial Cl atoms bridge four different Mn atoms to form two-dimensional $[MnCl_4]_n^{2-}$ inorganic layers, as shown in Fig. 4f.[92] Thus, the formula of 2D Mn(II) halide complexes is $AMnX_4$ with +2 A cation.

The d–d transition of Mn^{2+} in the centrosymmetric octahedral crystal field (O_h) is forbidden by the Laporte selection rule, leading to a low PLQY.[57] Thus, distortion of $[MnX_6]^{4-}$ octahedrons in the structure is necessary for red emissive Mn(II) halide complexes to achieve superior luminescence performance. Due to the diverse crystal structures, luminescent properties of red manganese halides are more complex than those of green manganese halides.

2.3.2 Optical properties of red Mn(II) halide complexes. Similar to tetrahedral $[MnX_4]^{2-}$ complexes, the optical properties of octahedral $[MnX_6]^{4-}$ systems arise from d-orbital splitting in O_h symmetry (Fig. 4h).[73] Excitation involves three characteristic energy regions: the lowest-energy $^6A_1(S)$ to $^4T_1(G)$ transition in the green region, intermediate $^6A_1(S)$ to $^4T_2(G)$, $^4A_1$, and $^4E(G)$ transitions, transitions in blue, and higher-energy $^6A_1(S)$ to $^4T_2(D)$, $^4E(D)$, and $^4T(P)$ transitions. The emission consistently originates from the $^4T_1(G)$ to $^6A_1(S)$ radiative transition (Fig. 4h and i).

This excitation–emission scheme persists across diverse structures: Wang *et al.* synthesized isolated 0D $(ABI)_4MnBr_6$ (629 nm, 80%),[17] with excitations from $^6A_1(S)$ to $^4T_1(G)$, $^4T_2(G)$, $^4A_1$, and $^4E(G)$ (525 nm, 374 nm and 440 nm) and $^6A_1(S)$ to $^4T_2(D)$ and $^4E(D)$ (340 nm and 365 nm). Wu *et al.* reported partially connected 0D $(Gua)_2MnCl_4$ (650 nm, 76%) with similar excitations.[83] Ju *et al.* demonstrated equivalent transitions in 1D $C_4H_{12}NMnCl_3$ (635 nm, 91.8%).[16]

The distinct photoluminescent properties of green- and red-emissive Mn(II) halide complexes fundamentally arise from differences in crystal field splitting within tetrahedral T_d $[MnX_4]^{2-}$ and octahedral O_h $[MnX_6]^{4-}$ coordination

Table 2 Comparisons of red Mn(II) complexes in structure and luminescent properties

Sample	Dimension	Peak/nm	PLQY/%	Stokes shift/nm	Closest Mn–Mn distance/Å	Δd/Å	$\Delta\theta$/°	Ref.
$(CH_6N_3)_2MnCl_4$	0D	642	69, 76	125	3.323	0.0057	4.65	83 and 85
$(ABI)_4MnBr_6$	0D	629	80	289	8.642	0.0086	—	17
$(ABI)_4MnCl_6$	0D	630	99	370	—	0.0413	3.50	82
$(MBI)MnCl_4\cdot H_2O$	1D	650	50	300	—	0.0260	3.93	
$(MBZI)(MnCl_3H_2O)\cdot H_2O$	1D	632	71	181	—	0.0253	4.09	21
$(C_8H_9N_2)_n\{(MnCl_3(H_2O)\cdot H_2O)\}_n$	1D	645	13	200	3.645	0.0251	3.95	89
$(TMSO)MnCl_3$	1D	629	86	~179	3.243	0.0069	6.00	90
$(TMSO)MnBr_3$	1D	626	58	~176	3.377	0.0075	4.93	
D-$(C_9H_{17}NO_2)[MnCl_3]$	1D	646	67	—	3.213	0.0081	5.69	86
L-$(C_9H_{17}NO_2)[MnCl_3]$	1D	656	57	—	3.210	0.0079	5.65	
$CsMnCl_3$	1D	644–665	42	—	4.1	0.0074	4.23	94

environments, governing both excitation and emission characteristics.[16,73,77] The associated Stokes shift between $^6A_1(S)$ to $^4T_1(G)$ excitation and $^4T_1(G)$ to $^6A_1(S)$ emission further correlates with these distinct geometries.[77] While Mn–Mn interatomic distances influence the photoluminescence quantum yield (PLQY) of six-coordinated Mn(II) halides by mitigating concentration quenching,[93] the luminescence efficiency in red-emitting systems is more critically governed by octahedral distortion, as mandated by the Laporte selection rule.

For instance, comparing 0D red manganese halides: $(ABI)_4MnBr_6$ achieves 80% PLQY (Mn–Mn > 8.74 Å),[17] compared to $(Gua)_2MnCl_4$ (76%, 8.551 Å)[83] and $CsMnCl_3$ (42%, 4.1 Å).[94] However, due to the divisive crystal structure of red manganese halides, the "concentration" of Mn is not a reliable parameter.[76] Different from green manganese halides, the Mn–Mn distance in red manganese halides is not the main influencing parameter. Paradoxically, 1D $CsMnCl_3$ exhibits a longer nearest Mn–Mn distance (4.1 Å) yet a lower PLQY (42%)[94] than $(TMSO)MnCl_3$ (3.24 Å, 86%)[90] and $(C_9H_{17}NO_2)[MnCl_3]$ (3.213 Å, 67%)[86] (Table 2), demonstrating that the Mn–Mn distance exerts a comparatively minor influence on the PLQY in red-emitting systems due to the Laporte selection rule. Furthermore, the significant PLQY difference between $(CH_3)_4NMnCl_3$ (94%) and $(CH_6N_3)_2MnCl_4$ (69%)[85] underscores the dominant role of distortion. As displayed in Table 2 and Fig. 5, the high-PLQYof red Mn halides consistently exhibit elevated bond-length (Δd) or bond-angle ($\Delta\theta$) distortion parameters (defined below), contrasting with green emitters where the Mn–Mn distance is paramount. This highlights the critical constraint of the Laporte rule on six-coordinated Mn(II) luminescence, necessitating significant focus on structural distortion.

$$\Delta d^2 = \frac{1}{6}\sum_{i=2}^{6}[(d_i - d_{ave})/d_{ave}]^2 \quad (1)$$

$$\Delta\theta^2 = \frac{1}{12}\sum_{i=1}^{12}[(\theta_i - 90^\circ)/90^\circ]^2 \quad (2)$$

where d_{ave} is the average Mn–Br bond lengths, d_i is the individual Mn–X (X = Cl, Br or O) bond length, and θ_i is a single Br–Mn–Br bond angle.

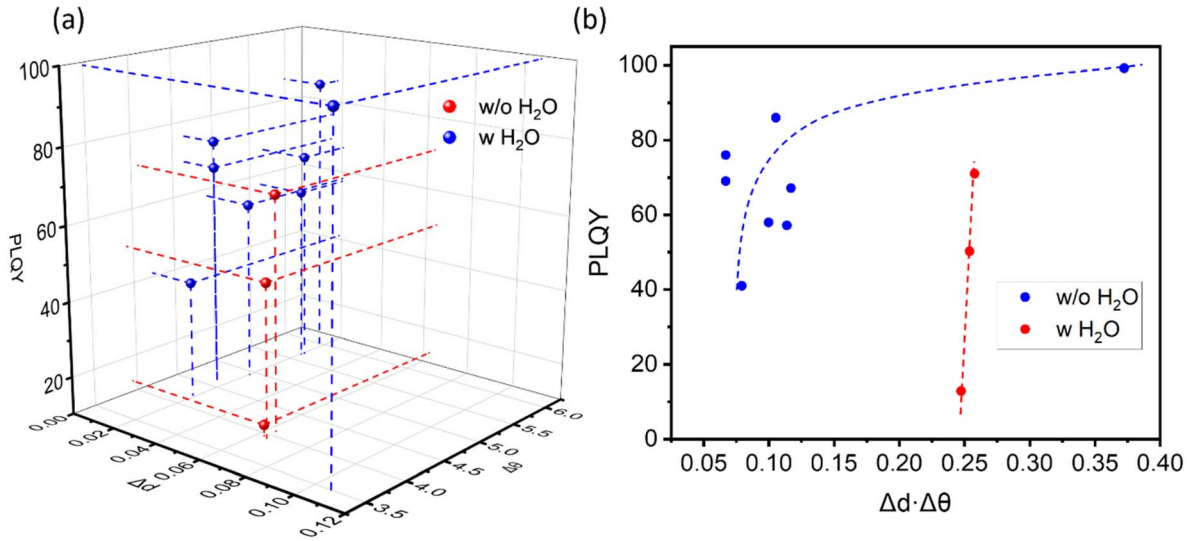

Fig. 5 PLQY and structure. (a) PLQY with Mn–X distance distortion (Δd) and X–Mn–X angle distortion ($\Delta\theta$). (b) PLQY with the composite parameter $\Delta d\cdot\Delta\theta$.

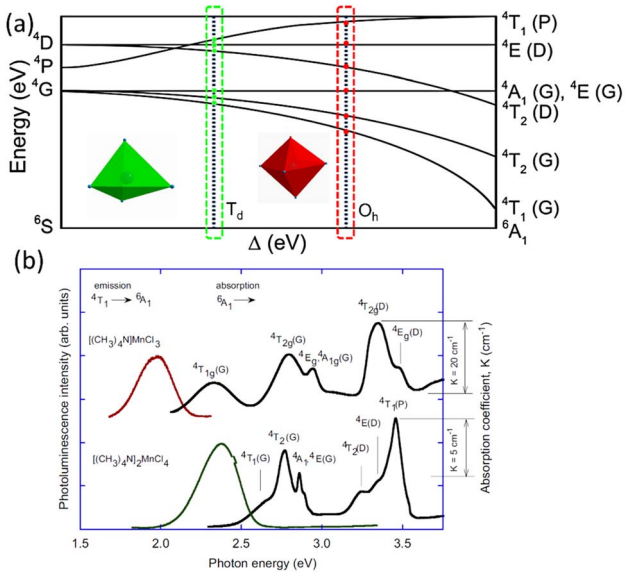

Fig. 6 (a) Tanabe–Sugano diagrams for Mn^{2+} ($3d^5$). (b) PL and PLE of green $[(CH_3)_4N]_2MnCl_4$ and red $[(CH_3)_4N]MnCl_3$. (a) Reproduced with permission from ref. 58. Copyright 2021, Wiley-VCH. (b) Reproduced with permission from ref. 73. Copyright 2009, Elsevier.

Compounds incorporating Mn–O bonds from H_2O ligands exhibit markedly higher Δd and $\Delta\theta$ values yet significantly reduced PLQY, warranting separate analysis of hydrated and anhydrous systems. To assess octahedral distortion, we introduce the composite parameter $\Delta d \cdot \Delta\theta$. The PLQY exhibits no monotonic dependence on Δd or $\Delta\theta$ alone (Table 2 and Fig. 5a). For example, $(TMSO)MnCl_3$ showed a higher PLQY (86%)[90] despite the lower Δd (0.0069 Å) than $CsMnCl_3$ (42%, 0.0074 Å).[94] Similarly, $(ABI)_4MnCl_6$ exhibited a higher PLQY (99%)[82] despite but a lower $\Delta\theta$ (3.5°) than $(C_9H_{17}NO_2)MnCl_3$.[86] The PLQY for red Mn halides demonstrates a monotonic increase with the composite distortion parameter $\Delta d \cdot \Delta\theta$ (Fig. 5b). Although hydrated compounds exhibit greater distortion, their PLQY is consistently lower, attributed to detrimental perturbations of the crystal field by O ligands. Furthermore, water-mediated structure regulation can introduce potential emission instability, causing luminescence fluctuations.

Therefore, achieving stable, high-efficiency red emission necessitates the use of anhydrous, halide-coordinated Mn(II) systems, where optimized octahedral distortion maximizes radiative efficiency within the constraints of the Laporte rule.

2.4 Structure regulation between red and green emissions

Emission mainly depends on the T_d and O_h ligand fields of Mn^{2+}, and thus changing the coordination environment of Mn^{2+} can influence the optical properties of Mn(II) halide complexes. For Mn(II) halide complexes with same components, changing the coordination geometry around Mn^{2+} from four-fold-coordinated $[MnX_4]^{2-}$ to six-fold-coordinated $[MnX_6]^{4-}$ changes the emission from green to red.[73,91] Furthermore, besides halides, O also participates in the crystal field according to Mn–O bonding and change the coordination number of Mn^{2+}, making Mn(II) complexes sensitive to environment.[64] The structure regulation between four Mn(II) complexes in T_d and O_h ligand fields expands potential applications for low-dimensional Mn(II) halide complexes.

The emission characteristics of Mn(II) halides are fundamentally governed by ligand field symmetry, where tetrahedral ($[MnX_4]^{2-}$) and octahedral ($[MnX_6]^{4-}$ or $[MnX_4L_2]^{2-}$) coordination geometries yield distinct green and red luminescence, respectively.[73,91] Phase transitions between these configurations

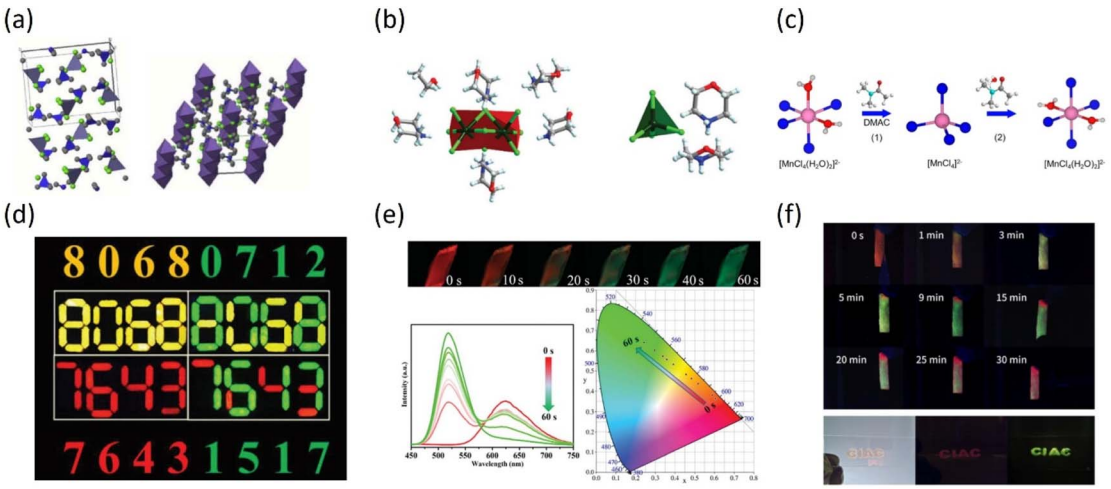

Fig. 7 Structure and luminescent properties of Mn(II) halide complexes with phase regulation between red and green emissions. (a) Crystal structure of green $(C_5H_6N)_2MnBr_4$ and red $C_5H_6NMnBr_3$. (b) Crystal structure of $(C_4NOH_{10})_5Mn_2Cl_9 \cdot C_2H_5OH$ and $(C_4NOH_{10})_2MnCl_4$. (c) Phase regulation between $Cs_2[MnX_4(H_2O)_2]$ and Cs_2MnX_4. (d) Photographs of the water-induced phase transformation process of $CsMnBr_3 : Pb^{2+}$ NCs under 365 nm UV light. (e) Thermo-chromic luminescence of $(C_4NOH_{10})_5Mn_2Cl_9 \cdot C_2H_5OH$ and $(C_4NOH_{10})_2MnCl_4$ under thermal treatment. (f) Photographs of test strips loaded with $Cs_2[MnX_4(H_2O)_2]$ powder after adding DMAC. (a) Reproduced with permission from ref. 73. Copyright 2009, Elsevier. (b and e) Reproduced with permission from ref. 61. Copyright 2019, Royal Society of Chemistry. (d) Reproduced with permission from ref. 96. Copyright 2024, Wiley-VCH. (c and f) Reproduced with permission from ref. 58. Copyright 2020, Wiley-VCH.

enable dynamic emission switching through three structural mechanisms, with optical responses quantifiable *via* crystal field parameters using Tanabe–Sugano diagrams (Fig. 6a).[57,73,77] This framework establishes that Racah parameters (B, C) describe the electron–electron repulsion, while crystal field splitting (Δ) determines the $^4T_1(G)$ excited-state energy. Crucially, $\Delta O_h > \Delta T_d$ positions $^4T_1(G)$ (T_d) energetically above $^4T_1(G)$ (O_h), explaining that the green-to-red emission shift is compositional in systems like $[(CH_3)_4N]_2MnCl_4$ (green) and $(CH_3)_4NMnCl_3$ (red),[77] with Stokes shifts scaling proportionally to Δ magnitude (Fig. 6b).

Structural transitions occur through: (1) solvent mediation, where molecules like ethanol in red-emitting $(C_4NOH_{10})_5Mn_2Cl_9\cdot C_2H_5OH$ template $[Mn_2Cl_9]^{5-}$ connectivity without direct Mn^{2+} coordination, with thermal removal yielding green-emitting $[MnCl_4]^{2-}$ (Fig. 7c and e).[61] (2) Direct ligand coordination, where H_2O converts $[MnX_4]^{2-}$ to distorted $[MnX_4(H_2O)_2]^{2-}$,[58,64,95] as demonstrated in hydration-driven transitions from red $CsMnBr_3:Pb^{2+}$ to green $Cs_3MnBr_5:Pb^{2+}$ nanocrystals (Fig. 7d).[22] While hydrated complexes typically exhibit red emission,[58] centrosymmetry-induced Laporte forbidden transition quenches luminescence, as evidenced by the PLQY reduction from 82% to 0% in hydrated $C_6N_2H_{16}MnBr_4$.[64] However, structural distortion enables anomalous blue emission[95] characterized by accelerated PL decay originating from sub-bandgap states, facilitating non-radiative recombination pathways, and enhanced electron–phonon coupling mediated by O–H vibrational modes in coordinated H_2O molecules. Dehydration restores original luminescence, confirming reversibility.[64]

These structure regulations enabled Mn(II) halides achieve predictable emission switching through well-defined structural mechanisms. Future research may: (1) quantify relationships between lattice strain, ligand covalency, and distortion metrics to enable rational material design; (2) explore distortion-engineered emission beyond conventional spectral ranges; (3) optimize switching cyclability for robust anti-counterfeiting and optical encryption technologies leveraging environmental sensitivity.[22,64,96]

3 Applications of Mn(II) halide complexes

Lead halide perovskites have become a new class of promising materials in optoelectronic devices due to their excellent optoelectronic properties.[1,2] Perovskites with the advantages of high luminescence performance, tunable emission and facile synthesis can achieve light-emitting diodes (LEDs) with high brightness, low cost, and wide color gamut for applications.[97–99] Along with the superior optoelectronic performance, the ability to form large, high-quality crystals and polycrystalline layers[100] makes lead halide perovskites some of the most promising materials for X-ray imaging technologies.[101] However, the toxicity and poor stability of lead perovskites have hindered their further application.

To overcome these obstacles, a series of lead-free luminescent metal halide complexes have been developed, featuring diverse coordination geometries centered on Bi^{3+}, Sb^{3+}, Cu^{+}, Sn^{2+}, and Zr^{4+} ions coordinated with halide ligands.[102–110] Some lead-free metal halide complexes exhibit high luminescence performance with PLQY above 90%, such as $(TEBA)_2SbCl_5$ (ref. 106) and $(C_9NH_{20})_2SbCl_5$,[105] which have been applied to white LEDs as phosphors. In addition to high PLQY, the large Stokes shift makes the lead-free metal halide complexes promising materials for radiation detection such as neutron[111] and X-ray imaging.[112–114]

However, the lead-free metal halide-based WLEDs can only be effectively pumped by a UV light-emitting diode chip with lower efficiency than the blue LED chip, leading to luminous efficacy loss of the LED.[16] Mn(II) halide complexes exhibit tunable green and red emissions by the crystal field and can be effectively pumped by the blue chip, making it suitable for LED applications.

3.1 Light emitting diodes

3.1.1 Mn(II) halide complexes as color conversion materials. According to the above description, Mn(II) halide complexes achieve high PLQYs in both green and red emissive regions and can be excited by blue light (400–500 nm) through the $^6A_1$ to ^4G transition. The superior luminescent properties and thermal stability make Mn(II) complexes promising materials for blue chip pumped white LED (WLED) applications.

As for green 0D Mn(II) halide complexes, the longer Mn–Mn distances in $[MnX_4]^{2-}$ lead to a high PLQY of near unity.[60,66] Thus, the four coordinated Mn(II) complexes are applied as green phosphor in the color conversion layer. A WLED can be fabricated by mixing the green-emitting Mn(II) phosphor and red-emitting $K_2SiF_6:Mn^{4+}$ (KSF) on a blue chip,[68,87] as shown in Fig. 8a. By mixing $(C_5H_6N)_2MnBr_4$ complexes with KSF, Deng *et al.* fabricated a WLED with an initial luminous efficacy of 93.90 lm W^{-1} on a blue InGaN chip (460 nm). The corresponding WLED displayed zero attenuation in emission intensity to 92.87 lm W^{-1} after continuous work for 410 minutes.[87] Xia *et al.* fabricated a WLED device by the $(C_{10}H_{16}N)_2MnBr_4$ and KSF phosphors on a blue InGaN chip (450 nm).[68] The WLED displayed a correlated color temperature (CCT) of 7218 K and a high luminous efficacy of up to 120 lm W^{-1} with the CIE chromaticity coordinates of (0.3054, 0.3088) located on the white region. The WLED covers a wide color gamut of 104% NTSC in CIE 1931 (Fig. 8b). The green $(C_{10}H_{16}N)_2MnBr_4$ phosphor showed no temperature quenching behaviour below 150 °C (Fig. 8c), which is attractive for use in the backlights of LCD devices.

The other way to achieve an LED from a conversion layer with a blue chip is by combining the green and red Mn(II) halide complexes in one layer. Different from the lead halide perovskites that fast anion exchange take place within 5 minutes in one layer,[87] emissions of Mn(II) halide complexes depend on T_d and O_h crystal fields and are stable in media with different compositions. Deng *et al.* fabricated LED devices through depositing a polystyrene (PS) film containing green emissive

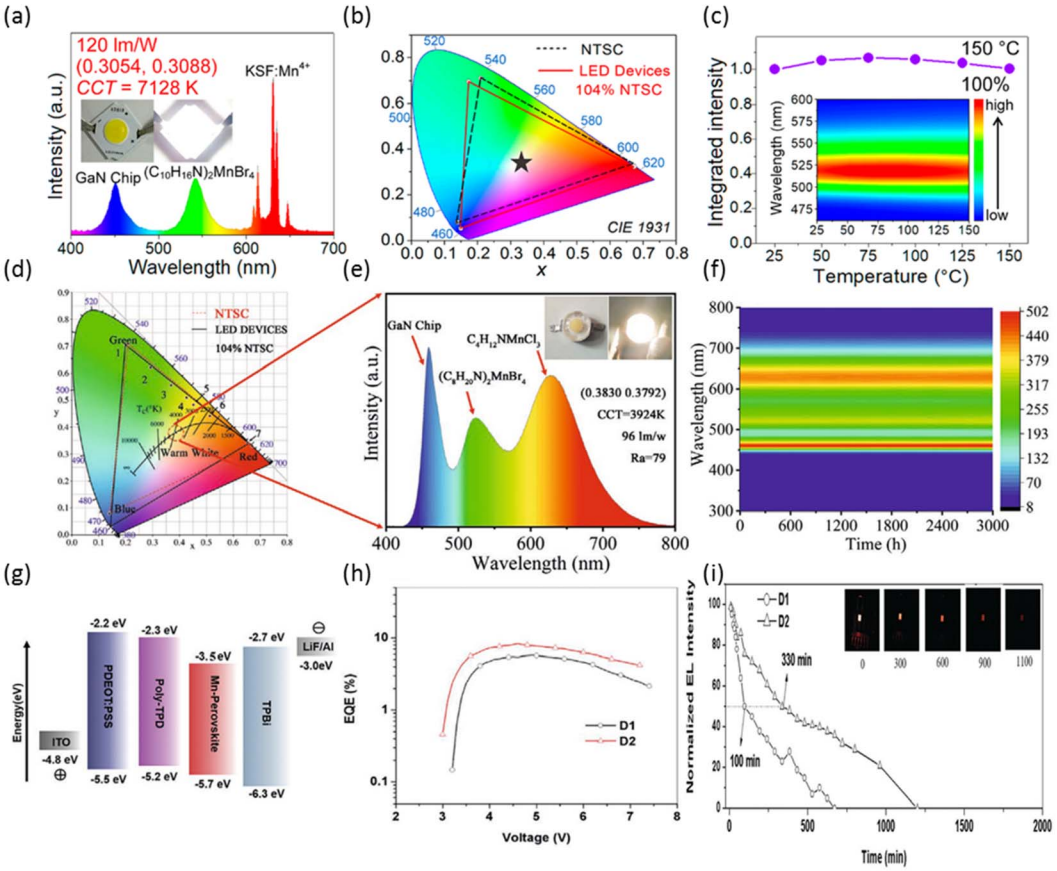

Fig. 8 Luminescent and stability properties of LEDs with Mn(II) halide complexes. (a) Emission spectrum of the white LED fabricated with $(C_{10}H_{16}N)_2MnBr_4$ and the $K_2SiF_6:Mn^{4+}$ phosphors on the InGaN chip ($\lambda_{em} = 450$ nm) at a 20 mA. The insets show the photographs of the device. (b) Color gamut of NTSC standard (black dotted line) and the fabricated white LED (red line, 104%) in the CIE 1931 system. (c) Integrated PL intensity of $(C_{10}H_{16}N)_2MnBr_4$ as a function of temperature. (d) Color gamut of NTSC standard (red dotted line) and the fabricated white LED (black line, 104%) in the CIE 1931 system. (e) Emission spectrum of the white LED using a blend of $C_4H_{12}NMnCl_3$ and $(C_8H_{20}N)_2MnBr_4$ on the InGaN chip ($\lambda_{em} = 460$ nm). The inset shows the photograph of the LED device with power off and on. (f) Integrated emission spectrum intensity of a white LED under operation as a function of time. (g) Bandgaps of the $(ABI)_4MnBr_6$ EL-LED. (h) EQEs of $(ABI)_4MnBr_6$ EL-LEDs at different voltages. (i) Stability of the $(ABI)_4MnBr_6$ EL-LED with a voltage of 5.0 V. (a–c) Reproduced with permission from ref. 68. Copyright 2020, American Chemical Society. (d–f) Reproduced with permission from ref. 16. Copyright 2021, Wiley-VCH. (g–i) Reproduced with permission from ref. 17. Copyright 2021, Wiley-VCH.

$(C_5H_6N)_2MnBr_4$ and red emissive $C_5H_6NMnCl_3$ phosphors on a blue chip.[87] The CRI and CCT can be further adjusted by changing the ratio between green and red Mn(II) halide phosphors. Similarly, Ju *et al.* fabricated a WLED based on a conversion layer consisting of $C_4H_{12}NMnCl_3$ and $(C_8H_{20}N)_2MnBr_4$.[16] The WLED exhibited an outstanding luminous efficacy of 96 lm W^{-1} and a wide color gamut of 104% NTSC in CIE 1931 (Fig. 8d and e). The corresponding PL peak positions and photoluminescence intensity showed no obvious decrease after 3000 hours under continuous operation (Fig. 8f).

3.1.2 Mn(II) halide complexes as emitting materials. Beyond serving as photoluminescent down-conversion phosphors, Mn(II) halide complexes can function directly as emissive layers in electroluminescent LEDs (hereafter termed EL-LEDs).[17,66] As shown in Fig. 8g, Mn(II) based EL-LEDs exhibit a layer structure. Chen *et al.* applied $(Ph_4P)_2MnBr_4$ doped with host materials TCTA and 26DCZPPY as an emitting layer, achieving a green EL-LED with a turn-on voltage of 4.8 V and a peak luminance of 2339 cd m^{-2} with an external quantum efficiency (EQE) of 9.6%.[66] Wang *et al.* fabricated a red EL-LED with EL emission at 627 nm with CIE color coordinates (0.69, 0.31) through 0D $(ABI)_4MnBr_6$.[17] The corresponding red EL-LED exhibited the maximum recording brightness of 4700 cd m^{-2} and EQE of 9.8%, as shown in Fig. 8h. The half-life of the device reached 5.5 h at 5 V (Fig. 8i), which showed superior performance among the lead free red EL-LEDs.[115]

Owing to the luminescent properties and stability, Mn(II) halide complexes are promising lead-free materials for both WLEDs and monochrome EL-LEDs.

3.1.3 Mn(II) halide complexes with circularly polarized luminescence. Beyond their conventional luminescent properties, manganese halides exhibit significant promise for applications in circularly polarized luminescent (CPL) materials.[116] CPL materials hold immense potential for advancing next-generation optoelectronic technologies, including circularly polarized light-emitting diodes (CP-LEDs),[65] three-dimensional

(3D) displays, CPL switches, and CPL detectors.[117,118] Manganese-based halides are particularly attractive candidates for high-performance CPL materials due to their exceptional photochemical stability, high photoluminescence quantum yields (PLQYs), low toxicity, and potential for incorporating additional functionalities such as ferroelectricity and magneto-chiroptical coupling.

Recent research has actively explored manganese halides as CPL emitters. Chen *et al.* synthesized chiral complexes (D)- and (L)-(*tert*-butyl prolinate)$MnCl_3$, achieving dissymmetry factors g of 6.1 × 10^{-3} and −6.3 × 10^{-3}, respectively.[86] Subsequently, Artem'ev *et al.* reported R/S-[MBA-Me_3]$MnBr_4$ with a g of 4.5 × 10^{-3}.[65] Chen *et al.* further demonstrated significantly enhanced performance in R/S-DACA$MnBr_3$,[119] achieving larger g values of 0.292 and 0.231. Notably, many CPL-active manganese halides, including 0D green emitters, exhibit one-dimensional long-range order in crystal structures.[67,120–122] This structural predisposition appears favorable for CPL generation. Given that red-emitting manganese halides also frequently adopt 1D structural motifs (Table 2), they demonstrate considerable potential for future CPL material development. Manganese halides emerge as highly promising platforms for circularly polarized luminescence, leveraging their inherent material advantages and structural versatility. The observed propensity for 1D crystal structures, common in both green- and red-emitting variants, coupled with recent demonstration of significant dissymmetry factors, underscores their strong potential for realizing efficient and functional CPL materials.

3.2 Radiation detection

3.2.1 Neutron imaging. Due to large Stokes shifts and high PLQYs, Mn-doped perovskite NCs have huge potential for fast neutron imaging. Fast neutrons are uncharged elementary particles with the kinetic elementary energy exceeding 1 MeV, which have low interaction cross sections and high penetration depths for both high- and low-Z elements. In contrast, other types of radiation sources, such as X-rays, γ-rays, and thermal neutrons, only respond to heavy or light elements. Therefore, fast neutron imaging is increasingly a nondestructive detection technology for large-scale samples of dense, mixed-Z compositions. However, the resolution of fast neutron imaging is still limited by conventional scintillator materials. In 2020, McCall *et al.* first reported a recoil proton detector based on colloidal semiconductor NCs in solvents with high hydrogen density.[111] It is noteworthy that Mn-doped $CsPbClBr_2$ perovskite NCs offer the best spatial resolution with 27 pixels because of the highest Stokes shift among a variety of semiconductor NCs tested. Subsequently, the same research group synthesized ultra-high concentration (>100 mg mL^{-1}) Mn-doped $CsPbClBr_2$ NCs through using 3-(*N*,*N*-dimethyloctadecylammonio)propanesulfonate (ACS18) as the zwitterionic ligand, promoting 8 times brighter light yield than oleyl-capped NCs under fast neutron irradiation.[43] Although Mn-doped $CsPbClBr_2$ NCs as a fast neutron scintillator have exhibited improved resolution and light yield, the liquid suspension is inconvenient to use for realistic imaging purposes. Another feasible strategy is that

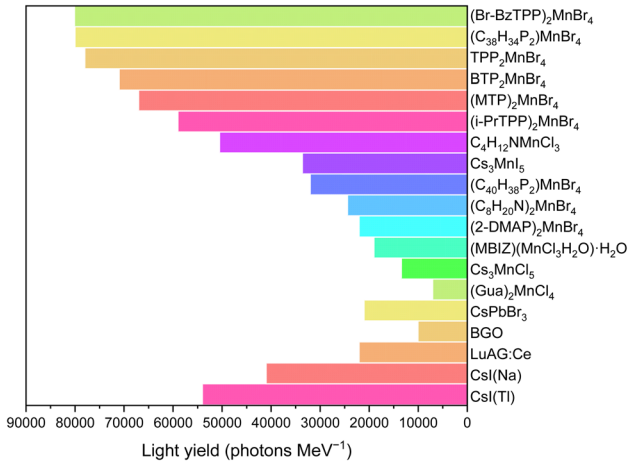

Fig. 9 Comparison of scintillator light yields of various Mn(II) complexes and previously reported and commercially available scintillators.

Zheng *et al.* proposed a single-component 2D Mn-doped $(C_{18}H_{37}NH_3)_2PbBr_4$ perovskite scintillator, in which hydrogen-rich organic components absorb fast neutrons and the dopant Mn^{2+} acts as luminescent centers in the perovskite that could offer a high Stokes shift and avoid self-absorption.[18] The Mn-doped $(C_{18}H_{37}NH_3)_2PbBr_4$ scintillator was finally made into imaging plates for fast neutron radiography with 0.5 lp mm^{-1} spatial resolution, but its light yield still falls behind the commercial ZnS(Ag) : PP scintillator screen. In the future, effective methods should be explored to enhance the interaction between Mn-doped perovskite and fast neutrons and improve its light yield.

3.2.2 X-ray imaging. As for X-ray imaging, a large Stokes shift is essential in order to avoid self-absorption within the relatively thick scintillating layer.[101] Mn(II) complexes exhibit a large Stokes shift for $^6A_1(S)$ to $^4T_1(G)$ excitation and the corresponding $^4T_1(G)$ to $^6A_1(S)$ emission, indicating a lower degree of self-absorption under X-ray excitation. The superior luminescent properties and large Stokes shift make Mn(II) complexes efficient X-ray scintillators for X-ray imaging.

As a group of low toxic candidate for X-ray scintillators, many Mn(II) complexes exhibit superior steady-state X-ray light yields than commercial BGO (10 000 photons per MeV), CsI : Tl (54 000 photons per MeV), CsI : Na (41 000 photons per MeV), LuAG : Ce (22 000 per photons MeV) and toxic $CsPbBr_3$ (21 000 photons per MeV),[123] as displayed in Fig. 9.[16,19,65,69,83,94,124] Among them, the green emissive $(C_{38}H_{34}P_2)MnBr_4$,[19] TPP_2MnBr_4,[125] (Br-BzTPP)$_2MnBr_4$ (ref. 71) and red emissive $C_4H_{12}NMnCl_3$ (ref. 16) Mn(II) complex X-ray scintillatiors have reached high light yields of 80 000 photons per MeV, 78 000 ± 2000 per photons MeV, 80 100 photons per MeV and 50 500 photons per MeV, respectively.

Another important parameter for scintillators is the evaluation of afterglow. A high afterglow can reduce the signal-to-noise ratio of X-ray imaging. Thus, it is always desirable to reduce the afterglow to obtain X-ray imaging with high contrast, especially for CT imaging. Compared with the commercial CsI : Tl (1.5% @ 3 ms), the Mn(II) complex X-ray scintillators exhibit a lower residual afterglow signal, as shown in Table 3.

Table 3 Comparisons of Mn(II) complex scintillators in light yield, detection limit, spatial resolution and afterglow

Material	Light yield/photons per MeV	Detection limit	Spatial resolution/lp mm^{-1}	Afterglow	References
S-[MBA-Me_3]$MnBr_4$	—	320 μGy s^{-1}	—	—	65
$(Gua)_2MnCl_4$	7000	145.3 nGy s^{-1}	8	BGO < $(Gua)_2MnCl_4$ < CsI(Tl)	83
Cs_3MnCl_5	13 400	470 μGy s^{-1}	4.0	—	94
(MBIZ)($MnCl_3H_2O$)·H_2O	19 000	204 nGy s^{-1}	11.1	30 ms(1%)	21
$(2\text{-DMAP})_2MnBr_4$	22 000	9.5 nGy s^{-1}	20–25	—	140
$(C_8H_{20}N)_2MnBr_4$	24 400	24.2 nGyair s^{-1}	5	2.06 ms(1%)	16
$(C_{40}H_{38}P_2)MnBr_4$	32 000	288 nGy s^{-1}	—	∼BGO	69
Cs_3MnI_5	33 600	400 nGy s^{-1}	7.45	—	124
$C_4H_{12}NMnCl_3$	50 500	36.9 nGyair s^{-1}	—	3.14 ms (1%)	16
$(i\text{-PrTPP})_2MnBr_4$	59 000	42.3 nGyair s^{-1}	46.6	—	72
$(MTP)_2MnBr_4$	67 000	28.1 nGyair s^{-1}	6.2	—	141
BTP_2MnBr_4	71 000	86.2 nGyair s^{-1}	23.8	—	142
TPP_2MnBr_4	78 000 ± 2000	8.8 nGy s^{-1}	15.7	3 ms (0.5%)	125
$(C_{38}H_{34}P_2)MnBr_4$	80 000	72.8 nGy s^{-1}	∼3	10 ms (to the background)	19
$(Br\text{-BzTPP})_2MnBr_4$	80 100	30 nGy s^{-1}	14.06	0.3 ms to baseline	71

The detection limit of X-ray dose rate required for X-ray medical diagnostics is 5.5 μGy S^{-1}.[126] For Mn(II) complex X-ray scintillators, the detection limit can reach as low as 8.8 nGy s^{-1},[125] which is about 625 times lower than the requirement. A high spatial resolution of 15.7 lp mm^{-1} was achieved in TPP_2MnBr_4 X-ray scintillation imaging, superior to the Eu^{3+} doped $CsPbBr_3$ glass-ceramic (10 000 photons per MeV and 15.0 lp mm^{-1})[127] and providing a higher light yield (Table 3). Furthermore, the Mn(II) complex can be imbedded in a flexible matrix such as PDMS to build a flexible scintillator with good resolution and expanding the corresponding application.[19]

Manganese(II) halide complexes have emerged as promising lead-free alternatives in optoelectronics, addressing the toxicity and stability limitations of lead halide perovskites despite their superior photophysical properties. While diverse lead-free metal halides (*e.g.*, based on Bi^{3+}, Sb^{3+}, and Cu^{+}) exhibit high PLQY and potential in radiation detection, their reliance on UV excitation limits the white light-emitting diode (WLED) efficiency. Mn(II) halides overcome this constraint through blue-light-excitable green/red emission tunable *via* crystal field engineering. For WLEDs, tetrahedral $[MnX_4]^{2-}$ complexes achieve near-unity PLQYs and serve as efficient color converters when blended with red phosphors on blue chips, delivering high luminous efficacy and thermal stability up to 150 °C. Alternatively, hybrid green/red Mn(II) phosphor layers in polymer matrices enable stable, tunable WLEDs with negligible efficiency decreasing after 3000 hours. Beyond photoluminescence, Mn(II) complexes function as electroluminescent emitters in LEDs, achieving green emission and red luminescence.

In radiation detection, the large Stokes shift of Mn halides minimizes self-absorption, enabling efficient X-ray scintillators with light yields (50 500–80 100 photons per MeV exceeding commercial scintillators, ultralow detection limits and high spatial resolution (Table 3). For neutron imaging, Mn-doped $CsPbClBr_2$ provides high spatial resolution *via* recoil proton detection,[43] while 2D Mn-doped lead halides offer solid-state alternatives despite the lower light yield.[18] Furthermore, chiral Mn(II) halides demonstrate significant circularly polarized luminescence (CPL) with dissymmetry factors up to 0.292,[81,127] attributed to their prevalent 1D structures and enabling applications in CP-LEDs, 3D displays, and optical switches.

Therefore, Mn(II) halides constitute a versatile, environmentally benign platform for advanced optoelectronics, excelling in blue-pumped WLEDs, high-resolution radiation detection, and chiroptical devices. This multifunctionality stems directly from their tunable emission, exceptional stability, and structurally adaptive coordination chemistry, positioning them as a cornerstone for sustainable photonic material innovation.

4 Conclusions and outlook

In this perspective, we have summarized the recent progress in Mn(II) complexes through their structures and luminescent properties. The properties of color tunability, high PLQYs, large Stokes shifts and thermal stability make Mn(II) complexes a class of promising materials for LEDs and radiation detection such as neutron and X-ray imaging.

Luminescent properties are mainly determined by the environment of the Mn^{2+} centre. The dopant Mn^{2+} exhibits orange emission in the lead halide perovskite host. The luminescent performances depend on the bandgap of the perovskite host and Mn^{2+} ion doping concentration. As for the green emissive Mn(II) halide phosphors, the emission and excitation are affected by the four-fold-coordinated $[MnX_4]^{2-}$ tetrahedron in a 0D structure. The PLQY of Mn(II) halides is primarily governed by Mn–Mn interatomic distances, the Stokes shift is modulated by angular distortion within the crystal structure and FWHM is determined by electron–phonon coupling influenced by structural distortions and organic A-site cations.[23,26,81,82] The red emission of Mn(II) complexes is derived from $[MnX_6]^{4-}$ octahedra through six-fold-coordinated $[MnX_6]^{4-}$ octahedra. The $[MnX_6]^{4-}$ octahedral units can connect through face-sharing and further crystallize into 0D and 1D structures. However, d–d transition of Mn^{2+} in the centrosymmetric octahedral crystal field is forbidden, leading to a low PLQY for red emissive Mn(II) complexes. Thus, distortion of $[MnX_6]^{4-}$ octahedra from both

the Mn–X length and X–Mn–X angle in the structure is necessary to achieve superior luminescence performance. Green emissive Mn(II) complexes with a PLQY near unity and red emissive Mn(II) complexes with a PLQY over 90% have already been achieved in previous research studies.

The luminescent properties, stability and low toxic nature of Mn(II) complexes make them suitable for LED and X-ray imaging applications. Mn(II) complexes are applied as color conversion materials on blue chips. The luminous efficacy of LEDs based on Mn(II) complexes and KSF phosphors reached up to 120 lm W^{-1}. The luminous efficacy of the LED fabricated by Mn(II) complexes as both green and red phosphors reached up to 96 lm W^{-1}. Besides, Mn(II) complexes can also be used as emitting materials in EL-LEDs. A red EL-LED with the maximum recording brightness of 4700 cd m^{-2} and EQE of 9.8% was achieved by $(ABI)_4MnBr_6$, which showed superior performance among the lead free red EL-LEDs. Manganese halides also exhibit promise for application in CPL materials,[116] which hold immense potential for advancing next-generation optoelectronic technologies, including circularly polarized light-emitting diodes (CP-LEDs),[65] three-dimensional (3D) displays, CPL switches, and CPL detectors.[117,118] Because of the large Stokes shift, Mn(II) complexes are thought to be promising materials for efficient radiation detection such as neutron and X-ray imaging. The spatial resolution for neutron scintillators reached 27 pixels by Mn-doped $CsPbClBr_2$ perovskite NCs. The currently prepared Mn(II) complex X-ray scintillators displayed the highest light yield of 80 000 photons per MeV, a spatial resolution of 25 lp mm^{-1} and the lowest detection limit of 8.8 nGy s^{-1}.

Although these results are encouraging, further improvements in Mn(II) complexes are still needed for both theoretical research and practical applications. (i) Material balancing efficiency and stability: the future development of Mn-based halides hinges on resolving the inherent trade-off between the PLQY and thermal and environmental stability. For both tetrahedrally coordinated green emitters and octahedrally coordinated red emitters, achieving a high PLQY requires sufficient Mn–Mn separation distances. Small inorganic cations may therefore not be suitable due to their tendency to decreasing Mn–Mn distance. Two strategies can address this challenge: Mn doping within octahedral/tetrahedral host frameworks[25] or incorporation of bulky rigid organic A-site cations,[81] enabling adequate Mn–Mn spacing while simultaneously enhancing material stability. (ii) Theoretically quantifying structure–property relationships: recently, Zhu *et al.*[85] has quantitatively correlated Mn octahedral distance mismatch with red emission efficiency in Mn-based halides. However, a quantitative or semi-quantitative understanding of how lattice distortions in high-symmetry octahedra govern excitonic behavior remains critical. For octahedrally coordinated red emitters, establishing correlations between crystallographic parameters (*e.g.*, bond length mismatch[85] and bond angle distortion[128]) and PLQYs will provide essential guidelines for designing efficient Mn-halide phosphors. Machine learning models that map crystallographic descriptors to optical outputs could further accelerate the discovery of high-performance red-emitting Mn halides. (iii) Application-driven innovations: colloidal Mn-based nanocrystals with narrow emission linewidths are essential for red and green color conversion layers in next-generation micro-LEDs.[129] A key advantage of Mn halides lies in their compatibility with high-temperature hot-injection methods, similar to lead halide perovskites, for synthesizing small-sized colloidal NCs. Advancing pixel-level patterning techniques for these nanomaterials could enable environmentally friendly color-conversion micro-LED technologies. Furthermore, Mn(II) halides have a high halogen content, showing promising prospects as scintillators. Developing highly luminescent Mn bromides/iodides with elevated atomic numbers (Z) may enable achieving efficient X-ray scintillators through enhanced photon attenuation and radiative recombination.

Manganese halides constitute a versatile, lead-free platform with tunable emission, large Stokes shifts, and exceptional stability. Future progress hinges on elucidating structure–distortion–property relationships, advancing synthetic control for environmental resilience, and pioneering device paradigms that leverage their unique photo-physics. Cross-disciplinary efforts integrating crystallography, spectroscopy, and device engineering will accelerate their deployment in next-generation optoelectronics and radiation detection.

Author contributions

The manuscript was written through contributions of all authors. All authors have given approval to the final version of the manuscript.

Conflicts of interest

There are no conflicts to declare.

Data availability

No primary research results, software or code has been included, and no new data were generated or analysed as part of this perspective.

Acknowledgements

This work was supported by National Natural Science Foundation of China (22075129).

Notes and references

1 A. K. Jena, A. Kulkarni and T. Miyasaka, Halide Perovskite Photovoltaics: Background, Status, and Future Prospects, *Chem. Rev.*, 2019, **119**, 3036–3103.
2 J. Shamsi, A. S. Urban, M. Imran, L. De Trizio and L. Manna, Metal Halide Perovskite Nanocrystals: Synthesis, Post-Synthesis Modifications, and Their Optical Properties, *Chem. Rev.*, 2019, **119**, 3296–3348.
3 J. Li, H.-L. Cao, W.-B. Jiao, Q. Wang, M. Wei, I. Cantone, J. Lü and A. Abate, Biological impact of lead from halide

perovskites reveals the risk of introducing a safe threshold, *Nat. Commun.*, 2020, **11**, 310.

4 Y. Li, Z. Shi, W. Liang, J. Ma, X. Chen, D. Wu, Y. Tian, X. Li, C. Shan and X. Fang, Recent advances toward environment-friendly photodetectors based on lead-free metal halide perovskites and perovskite derivatives, *Mater. Horiz.*, 2021, **8**, 1367–1389.

5 I. Infante and L. Manna, Are There Good Alternatives to Lead Halide Perovskite Nanocrystals?, *Nano Lett.*, 2021, **21**, 6–9.

6 A. Swarnkar, V. K. Ravi and A. Nag, Beyond Colloidal Cesium Lead Halide Perovskite Nanocrystals: Analogous Metal Halides and Doping, *ACS Energy Lett.*, 2017, **2**, 1089–1098.

7 R. N. Bhargava, D. Gallagher, X. Hong and A. Nurmikko, Optical properties of manganese-doped nanocrystals of ZnS, *Phys. Rev. Lett.*, 1994, **72**, 416–419.

8 V. Proshchenko and Y. Dahnovsky, Tunable Luminescence in CdSe Quantum Dots Doped by Mn Impurities, *J. Phys. Chem. C*, 2014, **118**, 28314–28321.

9 J. H. Yu, S.-H. Kwon, Z. Petrášek, O. K. Park, S. W. Jun, K. Shin, M. Choi, Y. I. Park, K. Park, H. B. Na, N. Lee, D. W. Lee, J. H. Kim, P. Schwille and T. Hyeon, High-resolution three-photon biomedical imaging using doped ZnS nanocrystals, *Nat. Mater.*, 2013, **12**, 359–366.

10 D.-Y. Jo, D. Kim, J.-H. Kim, H. Chae, H. J. Seo, Y. R. Do and H. Yang, Tunable White Fluorescent Copper Gallium Sulfide Quantum Dots Enabled by Mn Doping, *ACS Appl. Mater. Interfaces*, 2016, **8**, 12291–12297.

11 P. K. Santra and P. V. Kamat, Mn-Doped Quantum Dot Sensitized Solar Cells: A Strategy to Boost Efficiency over 5%, *J. Am. Chem. Soc.*, 2012, **134**, 2508–2511.

12 F. Carulli, F. Cova, L. Gironi, F. Meinardi, A. Vedda and S. Brovelli, Stokes Shift Engineered Mn:CdZnS/ZnS Nanocrystals as Reabsorption-Free Nanoscintillators in High Loading Polymer Composites, *Adv. Opt. Mater.*, 2022, **10**, 2200419.

13 C. S. Erickson, L. R. Bradshaw, S. McDowall, J. D. Gilbertson, D. R. Gamelin and D. L. Patrick, Zero-Reabsorption Doped-Nanocrystal Luminescent Solar Concentrators, *ACS Nano*, 2014, **8**, 3461–3467.

14 D. Parobek, B. J. Roman, Y. Dong, H. Jin, E. Lee, M. Sheldon and D. H. Son, Exciton-to-Dopant Energy Transfer in Mn-Doped Cesium Lead Halide Perovskite Nanocrystals, *Nano Lett.*, 2016, **16**, 7376–7380.

15 W. Liu, Q. Lin, H. Li, K. Wu, I. Robel, J. M. Pietryga and V. I. Klimov, Mn2+-Doped Lead Halide Perovskite Nanocrystals with Dual-Color Emission Controlled by Halide Content, *J. Am. Chem. Soc.*, 2016, **138**, 14954–14961.

16 T. Jiang, W. Ma, H. Zhang, Y. Tian, G. Lin, W. Xiao, X. Yu, J. Qiu, X. Xu, Y. Yang and D. Ju, Highly Efficient and Tunable Emission of Lead-Free Manganese Halides toward White Light-Emitting Diode and X-Ray Scintillation Applications, *Adv. Funct. Mater.*, 2021, **31**, 2009973.

17 S. Yan, W. Tian, H. Chen, K. Tang, T. Lin, G. Zhong, L. Qiu, X. Pan and W. Wang, Synthesis of 0D Manganese-Based Organic–Inorganic Hybrid Perovskite and Its Application in Lead-Free Red Light-Emitting Diode, *Adv. Funct. Mater.*, 2021, **31**, 2100855.

18 J. Zheng, Y. Zeng, J. Wang, C. Sun, B. Tang, Y. Wu, Y. Zhang, Y. Yi, N. Wang, Y. Zhao and S. Zhou, Hydrogen-Rich 2D Halide Perovskite Scintillators for Fast Neutron Radiography, *J. Am. Chem. Soc.*, 2021, **143**(50), 21302–21311.

19 L.-J. Xu, X. Lin, Q. He, M. Worku and B. Ma, Highly efficient eco-friendly X-ray scintillators based on an organic manganese halide, *Nat. Commun.*, 2020, **11**, 4329.

20 Q. Zhou, L. Dolgov, A. M. Srivastava, L. Zhou, Z. Wang, J. Shi, M. D. Dramićanin, M. G. Brik and M. Wu, Mn2+ and Mn4+ red phosphors: synthesis, luminescence and applications in WLEDs. A review, *J. Mater. Chem. C*, 2018, **6**, 2652–2671.

21 F. Yu, H.-R. Zhang, W.-W. Gao, C.-Y. Fang, Y.-N. Chen, M.-L. Xu, X.-W. Lei, X.-W. Kong and C.-Y. Yue, One-Dimensional Red Light–Emissive Organic Manganese(II) Halides as X-Ray Scintillators, *Inorg. Chem.*, 2024, **63**, 18146–18153.

22 J. Ren, L. Liu, H. Liu, X. Zhou, J. Li, F. Liu, L. Chen, G. Yan and Y. Wang, Lead-Doped Cesium Manganese Halide Perovskite Nanocrystals for Light-Emitting Diodes: Room-Temperature Synthesis, Energy Transfer, and Phase Modulating, *ACS Mater. Lett.*, 2025, **7**, 1028–1034.

23 D. D. Wang, H. M. Dong, L. L. Zhang, D. Wu, L. Y. Ren, D. X. Zhao, T. Wang and M. Feng, Yellow-Emitting Organic-Inorganic Hybrid Manganese Halides Realized by Br/Cl Composition Engineering, *Laser Photon. Rev.*, 2025, 2401982.

24 J. Hou, R. Liu, P. Han, C. Luo, Z. Ding, W. Zhou, C. Li, J. Li, Y. Zhao, J. Chen, J. Liu and B. Yang, Unveiling the Localized Exciton-Based Photoluminescence of Manganese Doped Cesium Zinc Halide Nanocrystals, *Nano Lett.*, 2023, **23**, 3762–3768.

25 Y. Yang, B. Ke, C. Yang, Y. Xue, K. Huang, X. Lu and B. Zou, Multifunctional applications enabled by tunable multi-emission and ultra-broadband VIS-NIR luminescence via energy transfer in Sn2+/Mn2+-doped lead-free Zn-based metal halides, *Mater. Horiz.*, 2025, **12**(8), 2564–2576.

26 B. He, B. Ke, C. Yang, Y. Chen, X. Zhong, W. Li and B. Zou, Efficient and Stable Red-Orange Emission from Polaronic Magnetic Excitons in Mn (II)-Doped 0D All-Inorganic Rb4CdCl6, *Adv. Opt. Mater.*, 2025, **13**, 2402624.

27 J. Ghosh, M. Hossain and P. K. Giri, Origin and tunability of dual color emission in highly stable Mn doped CsPbCl3 nanocrystals grown by a solid-state process, *J. Colloid Interface Sci.*, 2020, **564**, 357–370.

28 S. Oh, S. W. Bae, T. H. Kim, G. Kang, H. Jung, Y.-H. Kim and M. Park, Highly transparent all-perovskite luminescent solar concentrator/photovoltaic windows, *J. Mater. Chem. A*, 2024, **12**, 33193–33202.

29 X. Feng, Y. Sheng, K. Ma, F. Xing, C. Liu, X. Yang, H. Qian, S. Zhang, Y. Di, Y. Liu and Z. Gan, Multi-Level Anti-Counterfeiting and Optical Information Storage Based on Luminescence of Mn-Doped Perovskite Quantum Dots, *Adv. Opt. Mater.*, 2022, **10**, 2200706.

30 N. Pradhan, Red-Tuned Mn d–d Emission in Doped Semiconductor Nanocrystals, *ChemPhysChem*, 2016, **17**, 1087–1094.
31 D. Parobek, Y. Dong, T. Qiao and D. H. Son, Direct Hot-Injection Synthesis of Mn-Doped CsPbBr3 Nanocrystals, *Chem. Mater.*, 2018, **30**, 2939–2944.
32 Q. A. Akkerman, D. Meggiolaro, Z. Dang, F. De Angelis and L. Manna, Fluorescent Alloy CsPbxMn1–xI3 Perovskite Nanocrystals with High Structural and Optical Stability, *ACS Energy Lett.*, 2017, **2**, 2183–2186.
33 C.-W. Wang, X. Liu, T. Qiao, M. Khurana, A. V. Akimov and D. H. Son, Photoemission of the Upconverted Hot Electrons in Mn-Doped CsPbBr3 Nanocrystals, *Nano Lett.*, 2022, **22**, 6753–6759.
34 C. Orrison, J. R. Meeder, B. Zhang, J. Puthenpurayil, M. B. Hall, M. Nippe and D. H. Son, Efficient Redox-Neutral Photocatalytic Formate to Carbon Monoxide Conversion Enabled by Long-Range Hot Electron Transfer from Mn-Doped Quantum Dots, *J. Am. Chem. Soc.*, 2021, **143**, 10292–10300.
35 H. Liu, Z. Wu, J. Shao, D. Yao, H. Gao, Y. Liu, W. Yu, H. Zhang and B. Yang, CsPbxMn1–xCl3 Perovskite Quantum Dots with High Mn Substitution Ratio, *ACS Nano*, 2017, **11**, 2239–2247.
36 W. Q. Peng, S. C. Qu, G. W. Cong and Z. G. Wang, Concentration effect of Mn2+ on the photoluminescence of ZnS:Mn nanocrystals, *J. Cryst. Growth*, 2005, **279**, 454–460.
37 X. Yang, C. Pu, H. Qin, S. Liu, Z. Xu and X. Peng, Temperature- and Mn2+ Concentration-Dependent Emission Properties of Mn2+-Doped ZnSe Nanocrystals, *J. Am. Chem. Soc.*, 2019, **141**, 2288–2298.
38 S. Das Adhikari, A. Dutta, S. K. Dutta and N. Pradhan, Layered Perovskites L2(Pb1–xMnx)Cl4 to Mn-Doped CsPbCl3 Perovskite Platelets, *ACS Energy Lett.*, 2018, **3**, 1247–1253.
39 A. S. Silva, S. A. Lourenço and N. O. Dantas, Mn concentration-dependent tuning of Mn2+ d emission of Zn1−xMnxTe nanocrystals grown in a glass system, *Phys. Chem. Chem. Phys.*, 2016, **18**, 6069–6076.
40 A. De, N. Mondal and A. Samanta, Luminescence tuning and exciton dynamics of Mn-doped CsPbCl3 nanocrystals, *Nanoscale*, 2017, **9**, 16722–16727.
41 V. Naresh, M.-K. Cho, P.-R. Cha and N. Lee, Polar-Solvent-Free Sonochemical Synthesis of Mn(II)-Doped CsPbCl3 Perovskite Nanocrystals for Dual-Color Emission, *ACS Appl. Nano Mater.*, 2023, **6**, 4693–4706.
42 S. Zou, Y. Liu, J. Li, C. Liu, R. Feng, F. Jiang, Y. Li, J. Song, H. Zeng, M. Hong and X. Chen, Stabilizing Cesium Lead Halide Perovskite Lattice through Mn(II) Substitution for Air-Stable Light-Emitting Diodes, *J. Am. Chem. Soc.*, 2017, **139**, 11443–11450.
43 F. Montanarella, K. M. Mccall, K. Sakhatskyi, S. Yakunin, P. Trtik, C. Bernasconi, I. Cherniukh, D. Mannes, M. I. Bodnarchuk, M. Strobl, B. Walfort and M. V. Kovalenko, Highly Concentrated, Zwitterionic Ligand-Capped Mn2+:CsPb(BrxCl1–x)3 Nanocrystals as Bright Scintillators for Fast Neutron Imaging, *ACS Energy Lett.*, 2021, 4365–4373, DOI: **10.1021/acsenergylett.1c01923**.
44 S. Paul, E. Bladt, A. F. Richter, M. Döblinger, Y. Tong, H. Huang, A. Dey, S. Bals, T. Debnath, L. Polavarapu and J. Feldmann, Manganese-Doping-Induced Quantum Confinement within Host Perovskite Nanocrystals through Ruddlesden–Popper Defects, *Angew. Chem., Int. Ed.*, 2020, **59**, 6794–6799.
45 J. Zhu, X. Yang, Y. Zhu, Y. Wang, J. Cai, J. Shen, L. Sun and C. Li, Room-Temperature Synthesis of Mn-Doped Cesium Lead Halide Quantum Dots with High Mn Substitution Ratio, *J. Phys. Chem. Lett.*, 2017, **8**, 4167–4171.
46 L. Protesescu, S. Yakunin, M. I. Bodnarchuk, F. Krieg, R. Caputo, C. H. Hendon, R. X. Yang, A. Walsh and M. V. Kovalenko, Nanocrystals of Cesium Lead Halide Perovskites (CsPbX(3), X = Cl, Br, and I): Novel Optoelectronic Materials Showing Bright Emission with Wide Color Gamut, *Nano Lett.*, 2015, **15**, 3692–3696.
47 M. Imran, V. Caligiuri, M. Wang, L. Goldoni, M. Prato, R. Krahne, L. De Trizio and L. Manna, Benzoyl Halides as Alternative Precursors for the Colloidal Synthesis of Lead-Based Halide Perovskite Nanocrystals, *J. Am. Chem. Soc.*, 2018, **140**, 2656–2664.
48 S. Das Adhikari, S. K. Dutta, A. Dutta, A. K. Guria and N. Pradhan, Chemically Tailoring the Dopant Emission in Manganese-Doped CsPbCl3 Perovskite Nanocrystals, *Angew. Chem.*, 2017, **129**, 8872–8876.
49 S. Zhou, Y. Zhu, J. Zhong, F. Tian, H. Huang, J. Chen and D. Chen, Chlorine-additive-promoted incorporation of Mn2+ dopants into CsPbCl3 perovskite nanocrystals, *Nanoscale*, 2019, **11**, 12465–12470.
50 S. Das Adhikari, R. K. Behera, S. Bera and N. Pradhan, Presence of Metal Chloride for Minimizing the Halide Deficiency and Maximizing the Doping Efficiency in Mn(II)-Doped CsPbCl3 Nanocrystals, *J. Phys. Chem. Lett.*, 2019, **10**, 1530–1536.
51 A. Dutta, R. K. Behera, P. Pal, S. Baitalik and N. Pradhan, Near-Unity Photoluminescence Quantum Efficiency for All CsPbX3 (X=Cl, Br, and I) Perovskite Nanocrystals: A Generic Synthesis Approach, *Angew Chem. Int. Ed. Engl.*, 2019, **58**, 5552–5556.
52 Y. Li, C. Wang, G. Hu, W. Meng, S. Sui and Z. Deng, Promoting the doping efficiency and photoluminescence quantum yield of Mn-doped perovskite nanocrystals via two-step hot-injection, *Chem. Commun.*, 2022, **58**, 941–944.
53 Z. Deng, L. Tong, M. Flores, S. Lin, J.-X. Cheng, H. Yan and Y. Liu, High-Quality Manganese-Doped Zinc Sulfide Quantum Rods with Tunable Dual-Color and Multiphoton Emissions, *J. Am. Chem. Soc.*, 2011, **133**, 5389–5396.
54 Y. Li, S. Qi, P. Li and Z. Wang, Research progress of Mn doped phosphors, *RSC Adv.*, 2017, **7**, 38318–38334.
55 E. H. Song, Y. Y. Zhou, Y. Wei, X. X. Han, Z. R. Tao, R. L. Qiu, Z. G. Xia and Q. Y. Zhang, A thermally stable narrow-band green-emitting phosphor MgAl2O4:Mn2+ for wide color gamut backlight display application, *J. Mater. Chem. C*, 2019, **7**, 8192–8198.

56 Y. Zhu, Y. Liang, S. Liu, H. Li and J. Chen, Narrow-Band Green-Emitting Sr2MgAl22O36:Mn2+ Phosphors with Superior Thermal Stability and Wide Color Gamut for Backlighting Display Applications, *Adv. Opt. Mater.*, 2019, **7**, 1801419.

57 V. Morad, I. Cherniukh, L. Pöttschacher, Y. Shynkarenko, S. Yakunin and M. V. Kovalenko, Manganese(II) in Tetrahedral Halide Environment: Factors Governing Bright Green Luminescence, *Chem. Mater.*, 2019, **31**, 10161–10169.

58 H. Xiao, P. Dang, X. Yun, G. Li, Y. Wei, Y. Wei, X. Xiao, Y. Zhao, M. S. Molokeev, Z. Cheng and J. Lin, Solvatochromic Photoluminescent Effects in All-Inorganic Manganese(II)-Based Perovskites by Highly Selective Solvent-Induced Crystal-to-Crystal Phase Transformations, *Angew. Chem., Int. Ed.*, 2021, **60**, 3699–3707.

59 C. Jiang, N. Zhong, C. Luo, H. Lin, Y. Zhang, H. Peng and C.-G. Duan, Diisopropylammonium)2MnBr4: a multifunctional ferroelectric with efficient green-emission and excellent gas sensing properties, *Chem. Commun.*, 2017, **53**, 5954–5957.

60 M. Li, J. Zhou, M. S. Molokeev, X. Jiang, Z. Lin, J. Zhao and Z. Xia, Lead-Free Hybrid Metal Halides with a Green-Emissive [MnBr4] Unit as a Selective Turn-On Fluorescent Sensor for Acetone, *Inorg. Chem.*, 2019, **58**, 13464–13470.

61 M.-E. Sun, Y. Li, X.-Y. Dong and S.-Q. Zang, Thermoinduced structural-transformation and thermochromic luminescence in organic manganese chloride crystals, *Chem. Sci.*, 2019, **10**, 3836–3839.

62 L. Mao, P. Guo, S. Wang, A. K. Cheetham and R. Seshadri, Design Principles for Enhancing Photoluminescence Quantum Yield in Hybrid Manganese Bromides, *J. Am. Chem. Soc.*, 2020, **142**, 13582–13589.

63 H.-M. Pan, Q.-L. Yang, X.-X. Xing, J.-P. Li, F.-L. Meng, X. Zhang, P.-C. Xiao, C.-Y. Yue and X.-W. Lei, Enhancement of the photoluminescence efficiency of hybrid manganese halides through rational structural design, *Chem. Commun.*, 2021, **57**, 6907–6910.

64 H.-L. Liu, H.-Y. Ru, M.-E. Sun, Z.-Y. Wang and S.-Q. Zang, Organic−Inorganic Manganese Bromide Hybrids with Water-Triggered Luminescence for Rewritable Paper, *Adv. Opt. Mater.*, 2022, **10**, 2101700.

65 M. P. Davydova, L. Q. Meng, M. I. Rakhmanova, I. Y. Bagryanskaya, V. S. Sulyaeva, H. Meng and A. V. Artem'ev, Highly Emissive Chiral Mn(II) Bromide Hybrids for UV-Pumped Circularly Polarized LEDs and Scintillator Image Applications, *Adv. Opt. Mater.*, 2023, **11**, 2202811.

66 L.-J. Xu, C.-Z. Sun, H. Xiao, Y. Wu and Z.-N. Chen, Green-Light-Emitting Diodes based on Tetrabromide Manganese(II) Complex through Solution Process, *Adv. Mater.*, 2017, **29**, 1605739.

67 P. Tao, S.-J. Liu and W.-Y. Wong, Phosphorescent Manganese(II) Complexes and Their Emerging Applications, *Adv. Opt. Mater.*, 2020, **8**, 2000985.

68 G. Zhou, Z. Liu, J. Huang, M. S. Molokeev, Z. Xiao, C. Ma and Z. Xia, Unraveling the Near-Unity Narrow-Band Green Emission in Zero-Dimensional Mn2+-Based Metal Halides: A Case Study of (C10H16N)2Zn1–xMnxBr4 Solid Solutions, *J. Phys. Chem. Lett.*, 2020, **11**, 5956–5962.

69 T. Xu, W. Li, Z. Zhou, Y. Li, M. Nikl, M. Buryi, J. Zhu, G. Niu, J. Tang, G. Ren and Y. Wu, 0D Organic Manganese(II) Bromide Hybrids as Stable and Efficient X-Ray Scintillator, *Phys. Status Solidi Rapid Res. Lett.*, 2022, **16**, 2200175.

70 H. Dong, Y. Sun, L. Zhang, D. Wu, H. Shen, G. Pan, H. Wu, H. Wu, Z. Hao and J. Zhang, Near-Unity Narrow Green Emitting in Manganese Halides Realized by Direct Precipitation Synthesis, *Laser Photon. Rev.*, 2025, **19**, 2400365.

71 Z. Gong, J. Zhang, X. Deng, M.-P. Ren, W.-Q. Wang, Y.-J. Wang, H. Cao, L. Wang, Y.-C. He and X.-W. Lei, Near-unity broadband emissive hybrid manganese bromides as highly-efficient radiation scintillators, *Aggregate*, 2024, **5**, e574.

72 S. Chen, C. Guo, S.-C. Chen, Y. Di, X. Fang, M.-J. Lin and H. Yang, Enhanced Stability of Melt-Processable Organic–Inorganic Hybrid Manganese Halides for X-Ray Imaging, *Small*, 2024, **20**, 2406032.

73 Y. Rodríguez-Lazcano, L. Nataf and F. Rodríguez, Pressure-induced transformation from isolated MnX4(Td) to exchange-coupled MnX6(Oh) in A2MnX4 (X: Cl, Br) crystals. Structural correlations by time-resolved spectroscopy, *J. Lumin.*, 2009, **129**, 2000–2003.

74 B. Su, M. S. Molokeev and Z. Xia, Mn2+-Based narrow-band green-emitting Cs3MnBr5 phosphor and the performance optimization by Zn2+ alloying, *J. Mater. Chem. C*, 2019, **7**, 11220–11226.

75 A. Jana, S. Zhumagali, Q. Ba, A. S. Nissimagoudar and K. S. Kim, Direct emission from quartet excited states triggered by upconversion phenomena in solid-phase synthesized fluorescent lead-free organic–inorganic hybrid compounds, *J. Mater. Chem. A*, 2019, **7**, 26504–26512.

76 W. Zhang, W. Zheng, L. Li, P. Huang, J. Xu, W. Zhang, Z. Shao and X. Chen, Unlocking the Potential of Organic-Inorganic Hybrid Manganese Halides for Advanced Optoelectronic Applications, *Adv. Mater.*, 2024, **36**, 2408777.

77 Y. Rodríguez-Lazcano, L. Nataf and F. Rodríguez, Electronic structure and luminescence of ${[{({\text{CH}}_{3})}_{4}\text{N}]}_{2}\text{Mn}{X}_{4}$ $(X=\text{Cl},\text{Br})$ crystals at high pressures by time-resolved spectroscopy: pressure effects on the Mn-Mn exchange coupling, *Phys. Rev. B:Condens. Matter Mater. Phys.*, 2009, **80**, 085115.

78 S. Zhang, K. Han and Z. Xia, Pseudohalide Anions Driven Structural Modulation in Distorted Tetrahedral Manganese(II) Hybrids Toward Tunable Green-Red Emissions, *Angew. Chem., Int. Ed.*, 2025, **64**, e202419333.

79 Z. Qi, K. Zhang, X. Zhao, N. Zhang, S.-L. Li and X.-M. Zhang, Promoting structural distortion to enhance the crystal field strength of Mn(ii) in tetrahedral bromide for near-unity yellow emission, *Chem. Commun.*, 2024, **60**, 12880–12883.

80 Q. Ren, J. Zhang, Y. Mao, M. S. Molokeev, G. Zhou and X.-M. Zhang, Ligand Engineering Triggered Efficiency Tunable Emission in Zero-Dimensional Manganese

Hybrids for White Light-Emitting Diodes, *Nanomaterials*, 2022, **12**, 3142.
81 F. Yu, S. Y. Li, H. R. Yang, J. Shen, M. X. Yin, Y. R. Tian, Y. T. Zhang, X. W. Kong and X. W. Lei, Crystal-Rigidifying Strategy in Hybrid Manganese Halide to Achieve Narrow Green Emission and High Structural Stability, *Inorg. Chem.*, 2024, **63**, 14116–14125.
82 Y. Wang, T. Zhou, J. Chen, H. Qin, J. Wu, Z. Qin, H. Gu, Z. Gao, R. Liu, T. Ye, Y. Yang, F. Sun, T. Zhang, J. Hou, Y. Fang, Y. He, Y.-Y. Sun, M. Wang, L. Wang, H. Chen and W. Jiang, Flexible 3D printed fibers of novel manganese halides with superior acid/alkali resistance for X-ray imaging and radiation warning, *Chem. Eng. J.*, 2025, **515**, 163495.
83 W. Li, Z. Zhou, C. Wang, Y. Li, S. Kurosawa, G. Ren, X. OuYang and Y. Wu, Red-Emitting Organic–Inorganic Hybrid Manganese(II) Halides for X-Ray Imaging, *Adv. Sensor Res.*, 2023, **2**, 2200083.
84 X. Bai, H. Zhong, B. Chen, C. Chen, J. Han, R. Zeng and B. Zou, Pyridine-Modulated Mn Ion Emission Properties of C10H12N2MnBr4 and C5H6NMnBr3 Single Crystals, *J. Phys. Chem. C*, 2018, **122**, 3130–3137.
85 X. Zhu, X. Yan, E. Kang, Y. Han, C. Yin and S. Ye, Suppressing Energy Migration via Antiparallel Spin Alignment in One-Dimensional Mn2+ Halide Magnets with High Luminescence Efficiency, *Angew. Chem., Int. Ed.*, 2025, **64**, e202417218.
86 H.-L. Xuan, Y.-F. Sang, L.-J. Xu, D.-S. Zheng, C.-M. Shi and Z.-N. Chen, Amino-Acid-Induced Circular Polarized Luminescence in One-Dimensional Manganese(II) Halide Hybrid, *Chem.–Eur. J.*, 2022, **28**, e202201299.
87 G. Hu, B. Xu, A. Wang, Y. Guo, J. Wu, F. Muhammad, W. Meng, C. Wang, S. Sui, Y. Liu, Y. Li, Y. Zhang, Y. Zhou and Z. Deng, Stable and Bright Pyridine Manganese Halides for Efficient White Light-Emitting Diodes, *Adv. Funct. Mater.*, 2021, **31**, 2011191.
88 Y. Zhang, W.-Q. Liao, D.-W. Fu, H.-Y. Ye, C.-M. Liu, Z.-N. Chen and R.-G. Xiong, The First Organic–Inorganic Hybrid Luminescent Multiferroic: (Pyrrolidinium)MnBr3, *Adv. Mater.*, 2015, **27**, 3942–3946.
89 Y. Wu, X. Zhang, B. Zhang, L.-D. Xin, X.-M. Zhen and L.-J. Xu, Temperature/water triggered reversible emission transition in a one-dimensional Mn(ii)-based metal halide, *J. Mater. Chem. C*, 2024, **12**, 16471–16477.
90 X.-W. Kong, L.-X. Wu, X. Yang, D.-Y. Wang, S.-X. Wang, S.-Y. Li, C.-Y. Yue, F. Yu and X.-W. Lei, Enhancing the Water-Stability of 1D Hybrid Manganese Halides by a Cationic Engineering Strategy, *Adv. Opt. Mater.*, 2024, **12**, 2302710.
91 C. Li, X. Bai, Y. Guo and B. Zou, Tunable Emission Properties of Manganese Chloride Small Single Crystals by Pyridine Incorporation, *ACS Omega*, 2019, **4**, 8039–8045.
92 X.-H. Lv, W.-Q. Liao, P.-F. Li, Z.-X. Wang, C.-Y. Mao and Y. Zhang, Dielectric and photoluminescence properties of a layered perovskite-type organic–inorganic hybrid phase transition compound: NH3(CH2)5NH3MnCl4, *J. Mater. Chem. C*, 2016, **4**, 1881–1885.
93 D. Liang, H. Xiao, W. Cai, S. Lu, S. Zhao, Z. Zang and L. Xie, Mn2+-Based Luminescent Metal Halides: Syntheses, Properties, and Applications, *Adv. Opt. Mater.*, 2023, **11**, 2202997.
94 K. Li, W. Zhang, L. Niu, Y. Ye, J. Ren and C. Liu, Lead-Free Cesium Manganese Halide Nanocrystals Embedded Glasses for X-Ray Imaging, *Adv. Sci.*, 2023, **10**, 2204843.
95 Q. Kong, B. Yang, J. Chen, R. Zhang, S. Liu, D. Zheng, H. Zhang, Q. Liu, Y. Wang and K. Han, Phase Engineering of Cesium Manganese Bromides Nanocrystals with Color-Tunable Emission, *Angew. Chem., Int. Ed.*, 2021, **60**, 19653–19659.
96 S.-H. Xue, C.-M. Shi, L.-J. Xu and Z.-N. Chen, Thermal and Vapor Induced Triple-Mode Luminescent Switch of Manganese (II) Halides Hybrid, *Adv. Opt. Mater.*, 2024, **12**, 2302854.
97 X. Dai, Y. Deng, X. Peng and Y. Jin, Quantum-Dot Light-Emitting Diodes for Large-Area Displays: Towards the Dawn of Commercialization, *Adv. Mater.*, 2017, **29**, 1607022.
98 X. Wang, Z. Bao, Y.-C. Chang and R.-S. Liu, Perovskite Quantum Dots for Application in High Color Gamut Backlighting Display of Light-Emitting Diodes, *ACS Energy Lett.*, 2020, **5**, 3374–3396.
99 T. Hu, D. Li, Q. Shan, Y. Dong, H. Xiang, W. C. H. Choy and H. Zeng, Defect Behaviors in Perovskite Light-Emitting Diodes, *ACS Mater. Lett.*, 2021, **3**, 1702–1728.
100 R. K. Battula, C. Sudakar, P. Bhyrappa, G. Veerappan and E. Ramasamy, Single-Crystal Hybrid Lead Halide Perovskites: Growth, Properties, and Device Integration for Solar Cell Application, *Cryst. Growth Des.*, 2022, **22**(10), 6338–6362.
101 G. Kakavelakis, M. Gedda, A. Panagiotopoulos, E. Kymakis, T. D. Anthopoulos and K. Petridis, Metal Halide Perovskites for High-Energy Radiation Detection, *Adv. Sci.*, 2020, **7**, 2002098.
102 S. Liu, B. Yang, J. Chen, D. Wei, D. Zheng, Q. Kong, W. Deng and K. Han, Efficient Thermally Activated Delayed Fluorescence from All-Inorganic Cesium Zirconium Halide Perovskite Nanocrystals, *Angew. Chem., Int. Ed.*, 2020, **59**, 21925–21929.
103 C. Fang, J. Yang, G. Zhou, Z. Zhang, Y. Mao, X. Yun, L. Liu, D. Xu, X. Li and J. Zhou, Energy transfer from self-trapped excitons to rare earth ions in Cs2ZrCl6 perovskite variants, *J. Mater. Chem. C*, 2023, **11**, 1095–1102.
104 H. Peng, X. He, Q. Wei, Y. Tian, W. Lin, S. Yao and B. Zou, Realizing High-Efficiency Yellow Emission of Organic Antimony Halides via Rational Structural Design, *ACS Appl. Mater. Interfaces*, 2022, **14**(40), 45611–45620.
105 C. Zhou, H. Lin, Y. Tian, Z. Yuan, R. Clark, B. Chen, L. J. van de Burgt, J. C. Wang, Y. Zhou, K. Hanson, Q. J. Meisner, J. Neu, T. Besara, T. Siegrist, E. Lambers, P. Djurovich and B. Ma, Luminescent zero-dimensional organic metal halide hybrids with near-unity quantum efficiency, *Chem. Sci.*, 2018, **9**, 586–593.
106 Z. Li, Y. Li, P. Liang, T. Zhou, L. Wang and R.-J. Xie, Dual-Band Luminescent Lead-Free Antimony Chloride Halides

with Near-Unity Photoluminescence Quantum Efficiency, *Chem. Mater.*, 2019, **31**, 9363–9371.

107 M. Leng, Y. Yang, Z. Chen, W. Gao, J. Zhang, G. Niu, D. Li, H. Song, J. Zhang, S. Jin and J. Tang, Surface Passivation of Bismuth-Based Perovskite Variant Quantum Dots To Achieve Efficient Blue Emission, *Nano Lett.*, 2018, **18**, 6076–6083.

108 J.-H. Wei, J.-F. Liao, X.-D. Wang, L. Zhou, Y. Jiang and D.-B. Kuang, All-Inorganic Lead-Free Heterometallic Cs4MnBi2Cl12 Perovskite Single Crystal with Highly Efficient Orange Emission, *Matter*, 2020, **3**, 892–903.

109 T. Jun, K. Sim, S. Iimura, M. Sasase, H. Kamioka, J. Kim and H. Hosono, Lead-Free Highly Efficient Blue-Emitting Cs3Cu2I5 with 0D Electronic Structure, *Adv. Mater.*, 2018, **30**, 1804547.

110 J. Luo, M. Hu, G. Niu and J. Tang, Lead-Free Halide Perovskites and Perovskite Variants as Phosphors toward Light-Emitting Applications, *ACS Appl. Mater. Interfaces*, 2019, **11**, 31575–31584.

111 K. M. McCall, K. Sakhatskyi, E. Lehmann, B. Walfort, A. S. Losko, F. Montanarella, M. I. Bodnarchuk, F. Krieg, Y. Kelestemur, D. Mannes, Y. Shynkarenko, S. Yakunin and M. V. Kovalenko, Fast Neutron Imaging with Semiconductor Nanocrystal Scintillators, *ACS Nano*, 2020, **14**, 14686–14697.

112 J. Cao, Z. Guo, S. Zhu, Y. Fu, H. Zhang, Q. Wang and Z. Gu, Preparation of Lead-free Two-Dimensional-Layered (C8H17NH3)2SnBr4 Perovskite Scintillators and Their Application in X-ray Imaging, *ACS Appl. Mater. Interfaces*, 2020, **12**, 19797–19804.

113 W. Zhu, W. Ma, Y. Su, Z. Chen, X. Chen, Y. Ma, L. Bai, W. Xiao, T. Liu, H. Zhu, X. Liu, H. Liu, X. Liu and Y. Yang, Low-dose real-time X-ray imaging with nontoxic double perovskite scintillators, *Light: Sci. Appl.*, 2020, **9**, 112.

114 B. Yang, L. Yin, G. Niu, J.-H. Yuan, K.-H. Xue, Z. Tan, X.-S. Miao, M. Niu, X. Du, H. Song, E. Lifshitz and J. Tang, Lead-Free Halide Rb2CuBr3 as Sensitive X-Ray Scintillator, *Adv. Mater.*, 2019, **31**, 1904711.

115 Y. Yu, Y. Tang, B. Wang, K. Zhang, J.-X. Tang and Y.-Q. Li, Red Perovskite Light-Emitting Diodes: Recent Advances and Perspectives, *Laser Photon. Rev.*, 2023, **17**, 2200608.

116 K.-H. Jin, Y. Zhang, K.-J. Li, M.-E. Sun, X.-Y. Dong, Q.-L. Wang and S.-Q. Zang, Enantiomorphic Single Crystals of Linear Lead(II) Bromide Perovskitoids with White Circularly Polarized Emission, *Angew. Chem., Int. Ed.*, 2022, **61**, e202205317.

117 J. Ma, C. Fang, C. Chen, L. Jin, J. Wang, S. Wang, J. Tang and D. Li, Chiral 2D Perovskites with a High Degree of Circularly Polarized Photoluminescence, *ACS Nano*, 2019, **13**, 3659–3665.

118 J. Wang, C. Fang, J. Ma, S. Wang, L. Jin, W. Li and D. Li, Aqueous Synthesis of Low-Dimensional Lead Halide Perovskites for Room-Temperature Circularly Polarized Light Emission and Detection, *ACS Nano*, 2019, **13**, 9473–9481.

119 F. Wang, X. Li, T. Chen, L. Wang, C. Li, W. Zhang, W. Yuan, S. Lu, L. Li and X. Chen, A strategy of chiral cation coordination to achieve a large luminescence dissymmetry factor in 1D hybrid manganese halides, *Chem. Sci.*, 2025, **16**(24), 11012–11020.

120 M. P. Davydova, L. Meng, M. I. Rakhmanova, Z. Jia, A. S. Berezin, I. Y. Bagryanskaya, Q. Lin, H. Meng and A. V. Artem'ev, Strong Magnetically-Responsive Circularly Polarized Phosphorescence and X-Ray Scintillation in Ultrarobust Mn(II)–Organic Helical Chains, *Adv. Mater.*, 2023, **35**, 2303611.

121 J. Chen, S. Zhang, X. Pan, R. Li, S. Ye, A. K. Cheetham and L. Mao, Structural Origin of Enhanced Circularly Polarized Luminescence in Hybrid Manganese Bromides, *Angew. Chem., Int. Ed.*, 2022, **61**, e202205906.

122 C. Li, Y. Wei, Y. Li, Z. Luo, Y. Liu, M. He, Y. Zhang, X. He, X. Chang and Z. Quan, Manipulating Chiroptical Activities in 0D Chiral Hybrid Manganese Bromides by Solvent Molecular Engineering, *Small*, 2024, **20**, 2400338.

123 Y. Zhang, R. Sun, X. Ou, K. Fu, Q. Chen, Y. Ding, L.-J. Xu, L. Liu, Y. Han, A. V. Malko, X. Liu, H. Yang, O. M. Bakr, H. Liu and O. F. Mohammed, Metal Halide Perovskite Nanosheet for X-ray High-Resolution Scintillation Imaging Screens, *ACS Nano*, 2019, **13**, 2520–2525.

124 Q. Kong, X. Meng, S. Ji, Q. Wang, B. Yang, T. Bai, X. Wang, Z. Wang, R. Zhang, D. Zheng, F. Liu and K.-l. Han, Highly Reversible Cesium Manganese Iodine for Sensitive Water Detection and X-ray Imaging, *ACS Mater. Lett.*, 2022, **4**, 1734–1741.

125 K. Han, K. Sakhatskyi, J. Jin, Q. Zhang, M. V. Kovalenko and Z. Xia, Seed-Crystal-Induced Cold Sintering Toward Metal Halide Transparent Ceramic Scintillators, *Adv. Mater.*, 2022, **34**, 2110420.

126 H. Wei, Y. Fang, P. Mulligan, W. Chuirazzi, H.-H. Fang, C. Wang, B. R. Ecker, Y. Gao, M. A. Loi, L. Cao and J. Huang, Sensitive X-ray detectors made of methylammonium lead tribromide perovskite single crystals, *Nat. Photonics*, 2016, **10**, 333–339.

127 W. Ma, T. Jiang, Z. Yang, H. Zhang, Y. Su, Z. Chen, X. Chen, Y. Ma, W. Zhu, X. Yu, H. Zhu, J. Qiu, X. Liu, X. Xu and Y. Yang, Highly Resolved and Robust Dynamic X-Ray Imaging Using Perovskite Glass-Ceramic Scintillator with Reduced Light Scattering, *Adv. Sci.*, 2021, **8**, 2003728.

128 R. Chiara, M. Morana, M. Boiocchi, M. Coduri, M. Striccoli, F. Fracassi, A. Listorti, A. Mahata, P. Quadrelli, M. Gaboardi, C. Milanese, L. Bindi, F. De Angelis and L. Malavasi, Role of spacer cations and structural distortion in two-dimensional germanium halide perovskites, *J. Mater. Chem. C*, 2021, **9**, 9899–9906.

129 B.-R. Hyun, C.-W. Sher, Y.-W. Chang, Y. Lin, Z. Liu and H.-C. Kuo, Dual Role of Quantum Dots as Color Conversion Layer and Suppression of Input Light for Full-Color Micro-LED Displays, *J. Phys. Chem. Lett.*, 2021, **12**, 6946–6954.

130 S. Ji, X. Yuan, J. Li, J. Hua, Y. Wang, R. Zeng, H. Li and J. Zhao, Photoluminescence Lifetimes and Thermal

Degradation of Mn2+-Doped CsPbCl3 Perovskite Nanocrystals, *J. Phys. Chem. C*, 2018, **122**, 23217–23223.

131 S. Das Adhikari, S. K. Dutta, A. Dutta, A. K. Guria and N. Pradhan, Chemically Tailoring the Dopant Emission in Manganese-Doped CsPbCl3 Perovskite Nanocrystals, *Angew. Chem., Int. Ed.*, 2017, **129**, 8872–8876.

132 W. Liu, J. Zheng, S. Cao, L. Wang, F. Gao, K.-C. Chou, X. Hou and W. Yang, Mass production of Mn2+-doped CsPbCl3 perovskite nanocrystals with high quality and enhanced optical performance, *Inorg. Chem. Front.*, 2018, **5**, 2641–2647.

133 Y. Li, C. Wang, G. Hu, W. Meng, S. Sui and Z. Deng, Promoting the doping efficiency and photoluminescence quantum yield of Mn-doped perovskite nanocrystals via two-step hot-injection, *Chem. Commun.*, 2022, **58**, 941–944.

134 K. Xing, X. Yuan, Y. Wang, J. Li, Y. Wang, Y. Fan, L. Yuan, K. Li, Z. Wu, H. Li and J. Zhao, Improved Doping and Emission Efficiencies of Mn-Doped CsPbCl3 Perovskite Nanocrystals via Nickel Chloride, *J. Phys. Chem. Lett.*, 2019, **10**, 4177–4184.

135 J. Zhu, X. Yang, Y. Zhu, Y. Wang, J. Cai, J. Shen, L. Sun and C. Li, Room-Temperature Synthesis of Mn-Doped Cesium Lead Halide Quantum Dots with High Mn Substitution Ratio, *J. Phys. Chem. Lett.*, 2017, **8**, 4167–4171.

136 D. Chen, G. Fang, X. Chen, L. Lei, J. Zhong, Q. Mao, S. Zhou and J. Li, Mn-Doped CsPbCl3 perovskite nanocrystals: solvothermal synthesis, dual-color luminescence and improved stability, *J. Mater. Chem. C*, 2018, **6**, 8990–8998.

137 K. Xu, C. C. Lin, X. Xie and A. Meijerink, Efficient and Stable Luminescence from Mn2+ in Core and Core–Isocrystalline Shell CsPbCl3 Perovskite Nanocrystals, *Chem. Mater.*, 2017, **29**, 4265–4272.

138 W. J. Mir, M. Jagadeeswararao, S. Das and A. Nag, Colloidal Mn-Doped Cesium Lead Halide Perovskite Nanoplatelets, *ACS Energy Lett.*, 2017, **2**, 537–543.

139 Z.-J. Li, E. Hofman, A. H. Davis, A. Khammang, J. T. Wright, B. Dzikovski, R. W. Meulenberg and W. Zheng, Complete Dopant Substitution by Spinodal Decomposition in Mn-Doped Two-Dimensional CsPbCl3 Nanoplatelets, *Chem. Mater.*, 2018, **30**, 6400–6409.

140 Z. L. He, J. H. Wei, Z. Z. Zhang, J. B. Luo and D. B. Kuang, Manganese-Halide Single-Crystal Scintillator Toward High-Performance X-Ray Detection and Imaging: Influences of Halogen and Thickness, *Adv. Opt. Mater.*, 2023, **11**, 2300449.

141 W. Zhang, P. Sui, W. Zheng, L. Li, S. Wang, P. Huang, W. Zhang, Q. Zhang, Y. Yu and X. Chen, Pseudo-2D Layered Organic-Inorganic Manganese Bromide with a Near-Unity Photoluminescence Quantum Yield for White Light-Emitting Diode and X-Ray Scintillator, *Angew. Chem., Int. Ed.*, 2023, **62**, e202309230.

142 W. Shao, G. Zhu, X. Wang, Z. Zhang, H. Lv, W. Deng, X. Zhang and H. Liang, Highly Efficient, Flexible, and Eco-Friendly Manganese(II) Halide Nanocrystal Membrane with Low Light Scattering for High-Resolution X-ray Imaging, *ACS Appl. Mater. Interfaces*, 2023, **15**, 932–941.